NACA RM L53D10a

NACA

RESEARCH MEMORANDUM

ROCKET-MODEL INVESTIGATION OF THE LONGITUDINAL STABILITY, DRAG, AND DUCT PERFORMANCE OF A 60° DELTA-WING CANARD AIRCRAFT WITH TWIN SIDE INLETS AT MACH NUMBERS FROM 0.80 TO 1.70

By Aleck C. Bond and Andrew G. Swanson

Langley Aeronautical Laboratory
Langley Field, Va.

CLASSIFIED DOCUMENT

This material contains information affecting the National Defense of the United States within the meaning of the espionage laws, Title 18, U.S.C., Secs. 793 and 794, the transmission or revelation of which in any manner to an unauthorized person is prohibited by law.

NATIONAL ADVISORY COMMITTEE
FOR AERONAUTICS

WASHINGTON

March 29, 1954

NACA RM L53D10a

NATIONAL ADVISORY COMMITTEE FOR AERONAUTICS

RESEARCH MEMORANDUM

ROCKET-MODEL INVESTIGATION OF THE LONGITUDINAL STABILITY, DRAG, AND DUCT PERFORMANCE OF A 60° DELTA-WING CANARD AIRCRAFT WITH TWIN SIDE INLETS AT MACH NUMBERS FROM 0.80 TO 1.70

By Aleck C. Bond and Andrew G. Swanson

SUMMARY

A flight test was conducted by the Pilotless Aircraft Research Division of the Langley Aeronautical Laboratory on a rocket-boosted canard aircraft configuration having modified 60° delta lifting surfaces, twin normal-shock-type side inlets, and twin vertical tails. Drag, longitudinal-stability, and duct-performance data were obtained at Mach numbers from 0.80 to 1.70 covering a Reynolds number range of about 9×10^6 to 24×10^6, based on wing mean aerodynamic chord.

The lift-curve slope, static stability, and damping-in-pitch derivatives showed similar variations with Mach number, the parameters increasing from subsonic values in the transonic region and decreasing in the supersonic region. The variations were, for the most part, fairly smooth. The aerodynamic center of the configuration shifted rearward in the transonic region and moved forward gradually in the supersonic region. The pitching effectiveness of the canard control surfaces was maintained throughout the flight speed range, the supersonic values being somewhat greater than the subsonic. Trim values of angle of attack and lift coefficient changed abruptly in the transonic region, the change being associated with variations in the out-of-trim pitching moment, control effectiveness, and aerodynamic-center travel in this speed range. Duct total-pressure recovery decreased with increase in free-stream Mach number and the values were somewhat less than normal-shock recovery. Minimum drag data indicated a supersonic drag coefficient about twice the subsonic drag coefficient and a drag-rise Mach number of approximately 0.90. Base drag was small subsonically but was about 25 percent of the minimum drag of the configuration supersonically.

Comparison of the flight data with unpublished wind-tunnel data for the same configuration, in general, showed fair to good agreement. The

greatest differences between the flight and tunnel data were noted in the lift-curve slopes, and it was shown that the major portions of these differences resulted from aeroelastic effects on the wing and flexibility effects of the fuselage of the flight model.

INTRODUCTION

Because of the current interest in aircraft configurations employing canard control surfaces, the Langley Pilotless Aircraft Research Division is presently conducting an investigation of such a configuration by means of rocket-propelled models in free flight. The model reported in this paper has modified 60° delta lifting surfaces, twin normal-shock-type side inlets, and twin trapezoidal vertical tails. Drag, longitudinal stability, and duct performance of the configuration were investigated.

The basic aerodynamic parameters of the configuration were obtained by analysis of the dynamic response of the model to programmed pulses of the canard control surfaces and are presented over a Mach number range from 0.80 to 1.70 and a Reynolds number range from 9×10^6 to 24×10^6, based on wing mean aerodynamic chord.

SYMBOLS

A	area, sq ft
a_l	acceleration along reference axis as obtained from accelerometer, positive forward, ft/sec^2
a_n	acceleration normal to reference axis as obtained from accelerometer, ft/sec^2
b	wing span, ft
C_C	chord-force coefficient, $-\frac{a_l}{g}\frac{W}{qS}$
C_D	total drag coefficient, $C_C \cos \alpha + C_N \sin \alpha$
C_{D_B}	base drag coefficient, based on wing area
C_{D_i}	total internal drag coefficient, $\frac{2}{qS}\left[\dot{m}(V_o - V_x) + (p_o - p_x)A_x\right]$

[redacted]

$C_{D_{min}}$ total minimum drag coefficient of configuration

C_L lift coefficient, $C_N \cos \alpha - C_C \sin \alpha$

C_m pitching-moment coefficient about model center of gravity, based on wing area and wing mean aerodynamic chord

C_{m_O} pitching-moment coefficient at zero lift and zero canard control-surface deflection

$$C_{m_q} = \frac{\partial C_m}{\partial\left(\frac{q\bar{c}}{2V}\right)}$$

$$C_{m_{\dot{\alpha}}} = \frac{\partial C_m}{\partial\left(\frac{\dot{\alpha}\bar{c}}{2V}\right)}$$

C_N normal-force coefficient, $\frac{a_n}{g}\frac{W}{qS}$

C_p base pressure coefficient, $\frac{p_b - p_o}{q}$

$\bar{c}$ wing mean aerodynamic chord, ft

g acceleration due to gravity, ft/sec^2

H total pressure, lb/sq ft

l body length, ft

M Mach number

m mass flow through one duct, slugs/sec

m_o mass flow through a stream tube of area equal to inlet area of one duct under free-stream conditions, slugs/sec

P period of pitching oscillations, sec

p static pressure, lb/sq ft

p_b base pressure, lb/sq ft

[redacted]

q	free-stream dynamic pressure, $\frac{\gamma}{2} p_o M_o^2$, lb/sq ft
R	Reynolds number, based on wing mean aerodynamic chord
r	radius, ft
S	wing area (including area enclosed within the fuselage), sq ft
t	time, sec
$t_{1/2}$	time for pitching oscillations to damp to one-half amplitude, sec
V	velocity, ft/sec
V_c	velocity of sound, ft/sec
W	model weight, lb
x	longitudinal distance from station O, ft
y	lateral distance from center line of model, ft
α	angle of attack of reference axis, deg
α_o	angle of attack at zero lift and zero canard control-surface deflection, deg
γ	ratio of specific heats (1.40)
δ	angle between fuselage axis and canard chord measured in the plane of symmetry of the model, positive trailing edge down, deg
θ	angle of pitch, radians
ϕ	local wing twist angle produced by unit load applied perpendicular to wing chord at 50-percent chord line, positive leading edge up, radians/lb

Subscripts:

D	condition in duct
i	condition at duct inlet

[redacted]

o free-stream condition

$q = \frac{d\theta}{dt}$

SL sea-level standard condition (59° F and 2116 lb/sq ft)

T trim

x condition at duct exit

$\dot{\alpha} = \frac{1}{57.3}\frac{d\alpha}{dt}$

The symbols α and δ, when used as subscripts, denote the partial derivative of the quantity with respect to the subscript; for example, $C_{m_\alpha} = \frac{\partial C_m}{\partial \alpha}$.

MODEL AND APPARATUS

A sketch of the model used in the investigation is shown in figure 1 and photographs are shown as figure 2. The wing of the model was a modified 60° delta with the tips raked inward 30° resulting in an aspect ratio of 1.87. The wing was mounted on the lower part of the fuselage at 2° negative incidence to the fuselage reference line. The wing utilized a modified NACA 66-series airfoil section in the free-stream direction with a 2.83-percent thickness at the root chord (wing station zero) and a 6-percent thickness at the 87.26-percent semispan. Ordinates for sections at the 0- and 87.26-percent semispan stations are given in table I.

The canard control surfaces were geometrically similar in plan form to the wing but had 15° dihedral. A modified NACA 66-series airfoil section in the free-stream direction was utilized with a constant 5-percent-thickness ratio. Canard airfoil ordinates are given in table II. The axis of rotation was located at the 50.6-percent station of the canard mean aerodynamic chord.

The model had two vertical-tail surfaces of modified biconvex airfoil section, approximately 5 percent thick, mounted on the engine nacelles and displaced 25° outward from vertical. Ordinates for the tail surfaces are given in table III.

The model was equipped with twin sharp-lipped normal-shock-type side inlets with boundary-layer bleeds located forward of the entrance

[redacted]

lip. The interior duct lines made a gradual transition from the nearly circular inlet cross section to a circular cross section in approximately the first quarter of the duct length. From this point to the exit nozzle, the ducts continued circular and of constant diameter of 4 inches. The measured inlet areas of the left and right ducts were 6.10 square inches and 6.14 square inches, respectively. The boundary-layer bleeds located 0.91 inch ahead of the inlets were 0.26 inch in height and had measured areas of 0.75 square inch each. The boundary-layer mass flow was ducted to the free stream through three diverging passages, two of which exhausted on the upper side of the inlet and one exhausted on the lower side of the inlet. Details of the inlet and boundary-layer bleed system may be seen in figure 3. The mass flow through the ducts was controlled by the duct exit nozzles which were designed to allow passage of a mass flow ratio of approximately 0.9 through the inlet at peak Mach number. The exit nozzle was a simple convergent nozzle with a minimum diameter of 2.55 inches which gave a nozzle contraction ratio of 0.406. A view of the after end of the model showing the duct exits is shown in figure 4.

The basic body of the model was composed of a parabolic forebody and a cylindrical center section. Ordinates of the forebody and cylindrical section are given in table IV. The afterbody faired into the duct and wing lines as shown in figures 1, 2, and 3.

The model was constructed essentially of the following materials: wing, magnesium plate; canards, steel; vertical tails, aluminum-alloy casting; forward body, magnesium sheet; afterbody, magnesium casting; duct inlets, aluminum alloy.

The canard control surfaces were pulsed by a hydraulic servosystem in a square-wave motion from approximately -1.0° to -4.8°. The pulse rate of the canards was changed during the flight by means of a pressure-operated switch at a predetermined value of free-stream total pressure.

The model weighed 156.15 pounds and the moment of inertia in pitch was 20.39 slug-feet^2. The center of gravity of the model was at station 56.98 or at -12.32 percent of the mean aerodynamic chord. The vertical location of the center of gravity was 0.622 inch below the fuselage reference line.

INSTRUMENTATION

The model was equipped with a telemeter system which transmitted 12 channels of information of which 8 channels were continuous and 4 channels were switched. The eight continuous channels of information were longitudinal acceleration (high and low range), normal acceleration (high and low range), angle of attack, canard position, and two

base pressures. The switched channels transmitted pitot stagnation pressure, duct total pressure, duct nozzle static pressure, and a reference static pressure (included solely for use in determining flight Mach number in the event of failure of tracking radar). The accelerometers were mounted as near the center of gravity of the model as practical in order to keep the accelerometer corrections to a minimum. Angle of attack was measured by means of a vane-type instrument (ref. 1) located on a sting ahead of the nose of the model (fig. 1). The two base-pressure measurements were of (1) the pressure at essentially the center of the base and (2) the average pressure of four manifolded pressure orifices equally spaced about the exit of the left duct. Locations of the base-pressure orifices are shown in figure 5. Pitot stagnation pressure was measured by a total-pressure tube located on a small strut below the fuselage, as shown in figure 1. The reference static pressure measured was the pressure inside the cone of the angle-of-attack vane. The duct total pressure was measured just ahead of the exit nozzle by a six-tube manifolded total pressure rake as shown in figure 5. The pressure rake was inclined at an angle of 35° to the lateral axis of the model and the tubes were positioned on an equal area basis. An orifice located in the minimum section of the exit nozzle as shown in figure 5 was used to measure the duct nozzle static pressure. Because both ducts of the model were geometrically similar, only the left duct was instrumented.

A CW Doppler radar unit was used for obtaining checks on the model velocity and a tracking radar unit was employed for obtaining the model range, elevation, and azimuth as a function of time. Atmospheric conditions were determined from a radiosonde released at the time of firing. Fixed and manually operated 16-millimeter, 35-millimeter, and 70-millimeter cameras were employed to record the launching and the initial portion of the flight test.

TEST AND ANALYSIS PROCEDURES

Test

The model-booster combination was ground-launched at an angle of 55° from the horizontal from a mobile-type launcher as shown in figure 6. The model was boosted to a peak Mach number of 1.70 by a single-stage booster utilizing two 6-inch solid-fuel ABL Deacon rocket motors. Because of its lower drag-to-weight ratio, the model separated from the booster at rocket burnout. The model had no sustaining rocket motor and hence experienced decelerating flight after separation from the booster.

The data on the characteristics of the model were obtained during the decelerating portion of the flight. The model was disturbed in pitch by a programmed variation of the canards in an approximate square wave

pattern. The controls were set to operate between the limits of -4.8° and -1.0° at a rate of 1 cycle in 1.7 seconds during the supersonic portion of the flight (from separation to $M \approx 1$) and at a rate of 1 cycle in 3.1 seconds during the subsonic portion of flight. During the flight, the control position indicator showed that the canard remained at a fixed deflection after each pulse, but the deflection angles for both the high and low deflections after each pulse varied somewhat from the preset stop values. The incremental change in deflection for each pulse, however, remained essentially constant. A time-history of the canard deflection angle and Mach number is shown in figure 7. Behavior of the canard deflection in this manner indicates that the control position indicator or pulsing mechanism (or both) was being affected by the aerodynamic and inertial loading of the system in the longitudinal direction rather than in the normal direction. Play or flexibility in the various components of the system of approximately 0.025 inch would be sufficient to cause the observed shifts in stop position. Ground tests with an identical control system in an identical model failed to disclose any conclusive evidence as to the exact cause of the shifts. Since the canard deflection was constant after each pulse, the character of resulting oscillations was not changed, and hence the stability and damping data were not affected; however, the trim data may be less accurate because of the possible introduction of error in the value of the canard deflection angle.

The Reynolds numbers (based on the wing mean aerodynamic chord) obtained during the flight test are shown in figure 8 as a function of Mach number. Plots of the ratios $\frac{V_c}{V_{c_{SL}}}$ and $\frac{p_o}{p_{o_{SL}}}$ for the flight are presented in figure 9.

Analysis

The model velocity and free-stream conditions were determined by using radiosonde, tracking radar, and pitot stagnation pressure data. The CW Doppler radar obtained velocity data during the boost period, but failed to track the model immediately after separation, giving only intermittent velocity data; hence, these data were used where available to serve as a check on the model velocity.

The angles of attack measured by the vane on the nose of the model were corrected to angles of attack at the model center of gravity by the method of reference 1.

The short-period longitudinal oscillations resulting from deflection of the canards were analyzed by the method of reference 2 to obtain the trim, static and longitudinal stability, and lift characteristics of the model. Because the trim data were obtained for different values of δ

for each pulse, the values of $\left(\frac{\Delta\alpha}{\Delta\delta}\right)_{trim}$ and $\left(\frac{\Delta C_L}{\Delta\delta}\right)_{trim}$ were calculated by using the corresponding trim values at the end of a given pulse and beginning of the succeeding pulse. With the use of the calculated values, the trim characteristics at constant δ and the control effectiveness characteristics were calculated.

The base drag on the model was calculated by using the assumption that the base pressure measured by the manifolded pressure orifices was the average pressure over the annular base areas about the two duct exits and that the center base pressure measurement was the average pressure over the remainder of the base area. A sketch of the base of the model is shown in figure 5 illustrating the assumed proportioning of the base area.

The duct total-pressure recovery was obtained from a comparison of the measured duct total pressure with the free-stream total pressure. The mass-flow ratio was calculated using the relation

$$\frac{m}{m_o} = \frac{A_x}{A_i}\frac{p_x}{p_o}\frac{M_x}{M_o}\left(\frac{1 + \frac{\gamma - 1}{2}M_x^2}{1 + \frac{\gamma - 1}{2}M_o^2}\right)^{1/2}$$

The ratio of measured nozzle-exit static pressure to duct total pressure was used to indicate the transition from sonic to subsonic flow in the nozzle exit. The value of M_x was taken equal to 1.0 where the pressure ratio indicated sonic flow, whereas for subsonic flow, the value of M_x was determined directly from the pressure ratio. By assuming $H_x = H_D$, the value of p_x was determined from the pressure ratio p_x/H_x compatible with the value of M_x. The internal duct drag was calculated by considering the momentum and pressure differences in the entering stream tube from free stream to the duct exit and is represented by the expression

$$D = m(V_o - V_x) + (p_o - p_x)A_x$$

where the average value of V_x used was computed by means of one-dimensional compressible-flow theory.

The effects of wing flexibility on model lift-curve slope were determined by means of the method of reference 3 by using wing flexural properties (fig. 10) determined from a wing geometrically similar and

[redacted]

constructed of the same material as the wing of the flight model. The span loading employed was obtained from reference 4. Distribution of model lift was estimated by the use of unpublished wind-tunnel data for this configuration. Wing inertia effects were neglected in these calculations.

The effect of fuselage flexibility on the indicated angle of attack was estimated by determining the angular deviation of the nose of the model due to various loading conditions encountered in the flight. The aerodynamic loading was estimated by using the unpublished wind-tunnel data and the inertia loading was calculated from the flight data by using the design weight distributions of the model. The deflection of the fuselage was estimated by the use of unpublished fuselage static deflection data.

Accuracy

Possible systematic errors in the absolute level of directly measured quantities are proportional to the total range of the measuring instruments. On the basis of statistical data compiled by the Instrument Research Division of the Langley Aeronautical Laboratory, the instrumentation of this model is believed to be accurate to within ±1 percent of the full-scale range for pressure measuring instruments and $\pm 1\frac{1}{2}$ percent for the remaining instruments. Coefficients calculated from these directly measured quantities are subject to further errors resulting from possible inaccuracies in determination of atmospheric properties and model space position. For the flight ranges of this model, it is believed that combined errors of tracking radar and radiosonde data would result in possible errors of not more than ±1 percent of measured values of ambient pressure and temperature at the recorded altitude of the model if it is assumed that the atmospheric conditions encountered by the model are the same as those determined by the radiosonde.

Based on the aforementioned values, possible errors in the absolute values of quantities are as follows:

M	ΔM	ΔC_N	ΔC_C	ΔC_p	$\Delta \frac{H_D}{H_o}$	$\Delta\alpha$	$\Delta\delta$
1.7	±0.01	±0.002	±0.002	±0.01	±0.015	±0.45	±0.06
1.2	±.02	±.008	±.003	±.04	±.040	±.45	±.06
.8	±.04	±.016	±.004	±.07	±.075	±.45	±.06

[redacted]

These errors, systematic in nature, are dependent on radar and telemeter precision; therefore, relative values and parameters dependent upon slopes of measured quantities are, in general, more accurate than the foregoing would indicate. Derivatives, such as $C_{m_q} + C_{m_{\dot{\alpha}}}$ and C_{L_δ}, determined from mathematical relations of measured quantities, are of more questionable accuracy. Since the value of C_{m_α} is dependent to a greater extent on the period of oscillation, an approximation of the order of accuracy of this parameter may be determined from the scatter in the period data.

The angle-of-attack data are subject to an additional possible error of $\pm 0.5^\circ$ due to asymmetries, which may cause the vane to trim at angles to the airstream, and friction in the vane pivot, which may cause hysteresis loops in parameters varying with angle of attack. As mentioned in the section entitled "Test," there is an additional possible uncertainty in the canard deflection angle which could result in inaccuracies in the absolute level of trim data calculated at constant δ.

Single data points are subject to further inaccuracies due primarily to errors in reading the film records of the telemetered data. On the basis of statistical studies, approximately 90 percent of the points read should have an error of less than ± 1 percent (based on full-scale instrument range). These errors are random in nature and should be virtually eliminated in the final analysis by judicious fairing of the scatter in the test data points.

A discussion of some of the effects on accuracy of assumptions made in determining model characteristics by the pulse control technique, including neglected terms, acceleration effects, and effects of nonlinearities, is given in the appendixes of reference 2.

RESULTS AND DISCUSSION

In the following sections comparisons of the flight data are made, where possible, with existing unpublished wind-tunnel data of the same configuration as reported herein. These data were obtained from tests conducted in the 6- by 6-foot supersonic tunnel of the Ames Aeronautical Laboratory and will be hereinafter referred to simply as unpublished wind-tunnel data.

Lift

Plots of variation of lift coefficient with angle of attack for the first one or two oscillations following a control pulse are presented in

[redacted]

figure 11. The Mach number variation during these cycles was of the order of 0.03, the Mach numbers shown on the figure being the average ones for the data presented. The data for $M = 0.89$ are used for a portion of only 1 cycle because of excessive scatter in the data for the remainder of the oscillations for that pulse. The difference in C_L between increasing α and decreasing α probably results primarily from an angle-of-attack lag caused by friction in the vane system as mentioned in the section "Accuracy." Slopes do not appear to be appreciably affected by this displacement except near the peaks of the oscillations. The lift curves appear to be fairly linear within the angle-of-attack range covered, departures from linearity resulting, it is believed, from scatter in the experimental data.

Variation of lift-curve slope with Mach number as obtained from the lift plots is presented in figure 12. No significant variation was noted between data points at high and low canard deflection angles. The lift-curve slope increased from the subsonic value to a peak at $M = 1.05$ and then decreased smoothly with increase in Mach number.

Values of lift-curve slope from the unpublished wind-tunnel data are also presented in figure 12 for comparison. The values measured in free flight were of the order of 10 percent lower than the wind-tunnel data. It is believed that these differences are due largely to the differences in flexibility of the components of the two models and the differences in the dynamic pressures of the tests. The effects of wing aeroelasticity and fuselage flexibility on the model lift-curve slope were estimated as stated in the section entitled "Analysis" for the supersonic portion of the flight and are presented in figure 12 as reductions in C_{L_α} due to each. The reduction in C_{L_α} due to wing aeroelasticity is a relatively small quantity, approximately 2 percent of the measured C_{L_α}, whereas the reduction in C_{L_α} due to fuselage flexibility is of the order of two and a half times the magnitude of the wing aeroelastic effect. The dashed-line curve in figure 12, which represents the measured model lift-curve slope corrected for wing aeroelasticity and fuselage flexibility, shows closer correlation with the wind-tunnel data and hence tends to justify the belief that the observed differences between the wind-tunnel and flight data were largely due to differences in flexibility of the components of the respective models. Measured values of C_{L_α} were used in the calculation of parameters involving C_{L_α} except where noted.

Static Stability

The measured periods of pitching oscillations of the model, a measure of static stability, are presented in figure 13 as a function of Mach number. It is noted that there is no marked difference in the period as

[redacted]

determined at the high or low control deflections. These period data were used to calculate the static-stability derivative C_{m_α} which is presented in figure 14. Values of C_{m_α} increased negatively from the value at $M = 0.80$ to a peak at approximately $M = 1.05$ and then decreased gradually with increase in Mach number.

The variation with Mach number of the location of the missile aerodynamic center with and without corrections due to flexibility is presented in figure 15. The solid curve, which represents the aerodynamic-center location without flexibility corrections, was determined by using the measured C_{L_α} data of figure 12 and the C_{m_α} data of figure 14. The dashed-line curve represents the aerodynamic-center location corrected for fuselage flexibility and wing aeroelasticity. The correction for fuselage flexibility was accounted for by using the measured C_{L_α} corrected for fuselage flexibility, whereas the correction for wing aeroelasticity was determined using the method of reference 3. It might be noted that the latter correction was very small, less than 0.5 percent mean aerodynamic chord. The net effect of the two corrections is a slight forward shift in the aerodynamic center. Also shown in figure 15, for the purposes of comparison, are the aerodynamic-center locations determined from the unpublished wind-tunnel data and reduced to the flight model conditions for two control settings. The agreement of these data with the corrected flight data is considered to be good with the exception that the trends appear to differ at the higher Mach number.

Dynamic Stability

Dynamic-stability data were derived from the analysis of the damping of the short-period oscillation induced by the abrupt control deflection. Time to damp to one-half amplitude, determined from plots of amplitude ratios obtained from envelopes of the oscillation data, is shown in figure 16 as a function of Mach number. Data for the high control position show no significant variation from the data for the low control position. The values of the damping-in-pitch derivative $C_{m_q} + C_{m_{\dot{\alpha}}}$ determined from the $t_{1/2}$ data and the C_{L_α} data of figure 12, are presented in figure 17. The data corrected for the effects of fuselage flexibility on the measured C_{L_α} are also shown in figure 17 and indicate slightly less damping for the configuration. In addition to the experimental damping curve, the calculated damping curve for this configuration obtained from reference 5 is also included in figure 17. It is noted that, even though the calculated damping is considerably less than the experimental damping, the trend of the two curves with Mach number is very similar.

Longitudinal Control Effectiveness and Trim

The control derivatives C_{m_δ} and C_{L_δ} are presented in figures 18 and 19, respectively, along with corresponding data from the unpublished wind-tunnel tests of the configuration. The agreement is excellent over the range of speed covered in these tests. The lift due to canard deflection C_{L_δ} was essentially zero throughout the test range, with corrections for fuselage flexibility having negligible effect on the level of the data inasmuch as the corrected values are still essentially zero.

The variation of trim angle of attack and trim lift coefficient with Mach number as obtained from the flight test is presented in figure 20. Because the canard deflection limits were not consistent during the test, the measured values are included on the figures. The variations with Mach number of trim angle of attack per unit control deflection and trim lift coefficient per unit control deflection are presented in figure 21; the variations are smooth and indicate minimum values near $M = 1.05$. By the use of the aforementioned data, the trim angle of attack and trim lift coefficient were calculated for a constant δ of -5°, the curves of which are presented in figure 22. Included in figure 22 are the values of C_{L_T} obtained from the unpublished wind-tunnel data adjusted to the same center-of-gravity location as the flight model. These values agree very well with the flight data. These trim data indicate an abrupt and rather severe trim change in both lift coefficient and angle of attack between $M = 0.90$ and $M = 1.00$. This trim change is associated with the variations in out-of-trim pitching moment, change in control effectiveness, and center-of-pressure travel which occur in this speed range.

The variation of C_{m_0} with Mach number is presented in figure 23. The values of C_{m_0} were calculated from the following expression derived from the conventional moment equation:

$$C_{m_0} = \frac{-C_{m_\alpha}}{C_{L_\alpha}}\left(C_{L_T}\right)_{\delta=0}$$

Correcting C_{m_0} for the effects of fuselage flexibility tends to reduce its value slightly in the high-speed range. These corrected values show very good agreement with the unpublished wind-tunnel data. The data indicate a sharp increase in C_{m_0} between the Mach numbers of 0.9 and 1.0. The angle of attack for zero lift and zero control deflection α_0 was calculated by means of an expression derived from the lift equation of the model as

[redacted]

$$\alpha_0 = (\alpha_T)_{\delta=0} - \frac{(C_{L_T})_{\delta=0}}{C_{L_\alpha}}$$

and is presented in figure 24 as a function of Mach number. At the higher speeds, the level of the data calculated using the values of C_{L_α} corrected for fuselage flexibility is slightly higher than that obtained using the measured C_{L_α}, however, at the lower speeds the values are essentially the same. The flight data are of the order of 0.50° higher than the unpublished wind-tunnel data which are also plotted in figure 24. This difference may be the result of some out of trim of the vane, as noted in the section "Accuracy." The variation of α_0 with Mach number is similar to that of C_{m_0}.

Duct Performance

Duct-performance data are presented in figure 25 as functions of Mach number. The total-pressure recovery, measured at station 86.75 in the left duct of the model is presented in figure 25(a). A comparison of the measured total-pressure recovery with the normal-shock recoveries indicates losses of the order of 7 percent at $M = 1.7$ and 2 percent at $M = 1.0$ over normal-shock losses. Results of an experimental investigation of the performance characteristics of an inlet similar to that employed on the flight model are reported in reference 6. It is pointed out in this reference that the major portion of the losses occurring at the inlet are due to the high Mach numbers which were found to exist at the inlet. In addition, some losses were attributed to flow separation of the inlet. Total-pressure values reported in reference 6 for $M = 1.5$ and $M = 1.8$ and for corresponding mass flows are included in figure 25(a). These values of recovery agree very well with the flight data. A plot of the ratio of duct-exit nozzle static pressure to duct total pressure is presented in figure 25(b). This plot indicates that the exit nozzle was choked for all free-stream Mach numbers greater than 0.98 and the value of $M_x = 1.0$ was used for calculation of the mass-flow ratio over this speed range. The plot of the mass-flow ratio (fig. 25(c)) shows the mass-flow ratio increasing with Mach number up to a maximum of 0.88 at $M = 1.7$, which, it is estimated, would be a representative operational mass-flow ratio at this speed. The internal duct drag (fig. 25(d)) increases gradually in the Mach number range from $M = 1.0$ to $M = 1.7$. The values of the internal drag are very small in comparison with the total model drag, as shown subsequently. It was assumed that conditions in both ducts were the same, and the internal drag of the instrumented duct was doubled in order to arrive at the total internal drag of the model.

[redacted]

For the angle-of-attack range covered in the flight test, it was not possible to make any reasonable correlation of the variation of duct total-pressure recovery with angle of attack. The data indicated some small variations of total pressure with angle of attack; however, the variations were not consistent and were generally of the order of accuracy of the measuring instrument.

Base Pressure

Base pressure coefficients for the center orifice and manifolded orifice locations are presented in figure 26. These data show that the pressures about the duct exit were considerably lower than the pressures at the center of the base, especially during the supersonic portion of the flight. This effect is probably due to the influence of the flow issuing from the duct exit as well as the influence due to the external flow. The influence of flow issuing from a duct on base pressure is evidenced by the results of Cortright and Schroeder reported in reference 7. Their results have shown that the base pressures about an operating duct exit are reduced considerably from the power-off (no flow) values for certain low ranges of jet pressure ratio H_x/p_o. The jet pressure ratios of the flight model varied from approximately 1.90 to 3.90 in the speed range from $M = 1.0$ to $M = 1.7$ and are well within the range of pressure ratios for reduced base pressure. Presumably, the pressures at the center of the base are affected only slightly by the duct flow because of the further displacement of the center orifice from the duct exit and, hence, are probably of the same order of magnitude as would be obtained in a power-off condition.

Drag

Drag polars of the total drag are plotted in figure 27 for various average free-stream Mach numbers. Using the drag polars and extrapolations thereof, the minimum drag coefficient for the configuration (including base and internal drag) was determined; the minimum drag being taken at zero lift. The minimum drag coefficient, base-drag coefficient, and internal-drag coefficient are presented in figure 28 as functions of Mach number. Values of trim drag coefficient, obtained from plots of C_D against time, were used to complete the minimum-drag curve in the transonic region and to determine the drag-rise Mach number. This procedure was considered valid, because the trim lift of the model was reasonably low during this interval. The drag-rise Mach number determined in this manner is approximately 0.90. Minimum drag coefficient determined for high and low control deflection is indicated by use of different symbols in figure 28; no appreciable variation in the values of drag are noted for the two control positions. The base-drag-coefficient curve was

calculated as stated in the section "Analysis" using the base pressure coefficients of figure 26. This curve indicates very low base drag during the subsonic portion of flight and relatively high base drag (about 25 percent of minimum drag) during the supersonic portion. There is a slight dip in the curve at $M = 0.95$, and then the base drag begins to rise to a maximum at $M = 1.36$ and decreases gradually thereafter. The high base drag of the model is, of course, primarily due to the large base area of the model. Consideration of the mass-flow requirements dictated the size of the nozzle-exit areas and hence established the base area of the flight model. It is estimated that for an actual engine installation operating at the same mass-flow ratios as reported, the nozzle-exit areas would be increased by approximately a factor of 2 which would result in a decrease in base area of about 30 percent, with a corresponding decrease in base drag. The curve of internal-drag coefficient, originally presented in figure 25(d), is repeated in order to illustrate more clearly its small magnitude relative to the base and minimum drag coefficients. Also plotted in figure 28 is a curve of $C_{D_{min}} - C_{D_i} - C_{D_B}$ with two points from the unpublished wind-tunnel data shown for comparison. The wind-tunnel data have been corrected to zero base drag, but include the internal drag of the ducts; however, the internal drag coefficient of the wind-tunnel model should be of the same order of magnitude as that of the flight model, inasmuch as the mass-flow ratios were approximately the same. The agreement between the wind-tunnel and flight data is considered excellent and indicates negligible scale effect between the Reynolds numbers of approximately 20×10^6 (based on $\bar{c}$) of the flight-test data and 5×10^6 of the wind-tunnel data.

Because of the low range of lift coefficient obtained during the test, the induced drag factor dC_D/dC_L^2 and $(L/D)_{max}$ could not be precisely determined. The data indicated that dC_D/dC_L^2 was of the order of $\frac{1}{57.3C_{L_\alpha}}$.

In view of the current interest in the transonic area rule, plots of the longitudinal distribution of cross-sectional area and the equivalent body of revolution of the flight model are presented in figure 29. Subtracting the duct-inlet areas times 0.825 (the mass flow ratio at $M = 1.0$) from the total longitudinal cross-sectional area distribution resulted in an equivalent body of revolution of fineness ratio 8.73 with the maximum diameter at about 82.5 percent of the body length. As a matter of interest, a parabolic body of revolution having a fineness ratio of 8.91 and maximum diameter at 80 percent of the body length is also included in figure 29. The drag data for this body, reported in reference 8, indicated a drag-rise increment of about 0.021 (based on the wing area of the model reported herein) and a drag-rise Mach number of about 0.90 which is in good agreement with the drag-rise increment and drag-rise Mach number of the

[redacted]

configuration of this paper. This comparison is in accordance with the results of reference 9 which also show good agreement as to the drag-rise increment of several unswept and delta-wing airplane configurations and their equivalent bodies of revolution.

CONCLUDING REMARKS

A free-flight rocket-boosted model of a canard aircraft configuration having modified 60° delta lifting surfaces, twin normal-shock-type side inlets, and twin vertical tails has been flown at Mach numbers from 0.80 to 1.70. Data from the test indicate the following conclusions:

1. Lift-curve slope and static-stability parameter C_{m_α} varied smoothly with Mach number. The values increased from the subsonic values to a peak at a Mach number of 1.05 and then decreased gradually with increasing Mach number. The aerodynamic center shifted rearward from about 8 percent wing mean aerodynamic chord $\bar{c}$ at Mach number $M = 0.8$ to about 24.5 percent $\bar{c}$ at $M = 1.0$. There was a slight shift rearward at $M = 1.3$ and then a smooth forward movement to about 19 percent $\bar{c}$ at $M = 1.65$.

2. Pitching effectiveness C_{m_δ} of the canard control surface was maintained throughout the flight speed range, the supersonic values being somewhat higher than the subsonic, and lift effectiveness C_{L_δ} was essentially zero.

3. The model encountered abrupt trim changes in angle of attack and lift coefficient between Mach numbers 0.8 and 1.0, the change being associated with variations in the pitching-moment coefficient at zero lift and zero canard control-surface deflection C_{m_0}, pitching effectiveness C_{m_δ}, and center-of-pressure travel in this speed range. The values of the angle of attack at zero lift and zero canard control-surface deflection α_0 and C_{m_0} were fairly constant in the subsonic and supersonic range with an increase occurring in the region of $M = 0.9$ to $M = 1.0$.

4. Duct total pressure was about 7 percent less than normal-shock recovery at $M = 1.7$ and about 2 percent less at $M = 1.0$. The internal drag of the ducts was a small portion of the total drag. For the angle-of-attack range covered, there was no appreciable variation of duct total pressure with angle of attack.

5. Minimum drag coefficient was of the order of 0.02 subsonically and 0.04 supersonically. The drag-rise Mach number was approximately 0.9.

[redacted]

Base drag was rather small subsonically, but was about 25 percent of the minimum drag supersonically.

6. Comparison of the flight data with unpublished wind-tunnel data for the same configuration, in general, showed good agreement. It was shown that the differences between wind-tunnel and flight lift-curve slopes were due in greater part to aeroelastic effects on the wing and flexibility effects of the fuselage of the flight model.

Langley Aeronautical Laboratory,
National Advisory Committee for Aeronautics,
Langley Field, Va., April 16, 1953.

[redacted]

REFERENCES

1. Mitchell, Jesse L., and Peck, Robert F.: An NACA Vane-Type Angle-of-Attack Indicator for Use at Subsonic and Supersonic Speeds. NACA RM L9F28a, 1949.

2. Gillis, Clarence L., Peck, Robert F., and Vitale, A. James: Preliminary Results From a Free-Flight Investigation at Transonic and Supersonic Speeds of the Longitudinal Stability and Control Characteristics of an Airplane Configuration With a Thin Straight Wing of Aspect Ratio 3. NACA RM L9K25a, 1950.

3. Vitale, A. James: Effects of Wing Elasticity on the Aerodynamic Characteristics of an Airplane Configuration Having 45° Sweptback Wings As Obtained From Free-Flight Rocket-Model Tests at Transonic Speeds. NACA RM L52L30, 1953.

4. DeYoung, John, and Harper, Charles W.: Theoretical Symmetric Span Loading at Subsonic Speeds for Wings Having Arbitrary Plan Form. NACA Rep. 921, 1948.

5. Gillis, Clarence L., and Chapman, Rowe, Jr.: Summary of Pitch-Damping Derivatives of Complete Airplane and Missile Configurations As Measured in Flight at Transonic and Supersonic Speeds. NACA RM L52K20, 1953.

6. Dryer, Murray, and Beke, Andrew: Performance Characteristics of a Normal-Shock Side Inlet Located Downstream of a Canard Control Surface at Mach Numbers of 1.5 and 1.8. NACA RM E52F09, 1952.

7. Cortright, Edgar M., Jr., and Schroeder, Albert H.: Investigation at Mach Number 1.91 of Side and Base Pressure Distributions Over Conical Boattails Without and With Jet Flow Issuing From Base. NACA RM E51F26, 1951.

8. Hart, Roger G., and Katz, Ellis R.: Flight Investigations at High-Subsonic, Transonic, and Supersonic Speeds To Determine Zero-Lift Drag of Fin-Stabilized Bodies of Revolution Having Fineness Ratios of 12.5, 8.91, and 6.04 and Varying Positions of Maximum Diameter. NACA RM L9I30, 1949.

9. Hall, James Rudyard: Comparison of Free-Flight Measurements of the Zero-Lift Drag Rise of Six Airplane Configurations and Their Equivalent Bodies of Revolution at Transonic Speeds. NACA RM L53J21a, 1953.

[redacted]

TABLE I.- WING AIRFOIL ORDINATES

[Stations and ordinates given in percent of local chord. Upper ordinate equals lower ordinate.]

Wing root		87.26 percent semispan
Station	Ordinate	Ordinate
0	0	0
.5	.216	.460
1.25	.325	.690
2.5	.433	.920
5	.597	1.265
7.5	.723	1.533
10	.823	1.744
15	1.004	2.127
20	1.130	2.395
25	1.242	2.625
30	1.312	2.780
40	1.403	2.970
45	1.420	3.000
50	1.411	2.989
55	1.385	2.932
60	1.329	2.817
70	1.095	2.318
80	.796	1.648
90	.502	.996
95	.351	.671
100	.203	.345
L.E. radius = 0.020 in.		L.E. radius = 0.020 in.

[redacted]

TABLE II.- CANARD AIRFOIL ORDINATES

[Stations and ordinates given in percent of local chord. Upper ordinate equals lower ordinate.]

Station	Ordinate
0	0
.5	.393
.75	.464
1.25	.578
2.5	.764
5	1.050
7.5	1.270
10	1.475
15	1.770
20	2.000
25	2.185
30	2.320
40	2.480
45	2.500
50	2.495
60	2.350
70	1.935
Straight line to trailing edge	
100	0.035
L.E. radius = 1.55 percent local chord	

[redacted]

TABLE III.- VERTICAL-TAIL ORDINATES

[Stations and ordinates given in percent of local chord. Upper ordinates equals lower ordinates.]

Root chord (10.800 in. from tip)		Tip chord
Station	Ordinate	Ordinate
0	0	0
.75	.102	.143
1.25	.118	.190
2.5	.269	.309
5	.501	.547
10	.918	.952
15	1.290	1.309
20	1.614	1.618
25	1.883	1.904
30	2.106	2.118
40	2.403	2.404
50	2.496	2.500
60	2.403	2.404
70	2.106	2.118
75	1.883	1.904
81	1.549	1.571
Straight line to trailing edge		
100	0.390	0.428
L.E. radius = 0.004 in.		

[redacted]

TABLE IV.- FOREBODY AND CYLINDRICAL-SECTION ORDINATES

Body station, in.	Radius, in.
0	0
1.20	.198
3.00	.579
6.00	.941
9.00	1.356
12.00	1.759
15.00	2.121
18.00	2.453
21.00	2.754
24.00	3.025
27.00	3.264
30.00	3.473
33.00	3.651
36.00	3.798
39.00	3.914
42.00	4.000
45.00	4.055
48.80	4.080

Cylindrical section extends from body station 48.84 to station 67.20. After body lines fair into wing and ducts.

[redacted]

WING

Aspect ratio	1.87
Area (including fuselage)	6.12 sq ft
Area (exposed)	3.33 sq ft
Dihedral	0.0 deg
Incidence	-2.0 deg
M.A.C.	26.94 in.

CANARD

Aspect ratio (projected span and area)	1.78
Area (total)	1.08 sq ft
Area (projected exposed)	0.56 sq ft
Dihedral	15.0 deg
M.A.C.	7.87 in.

VERTICAL TAIL

Area (total exposed)	1.19 sq ft
Dihedral	65.0 deg
Incidence	0.0 deg

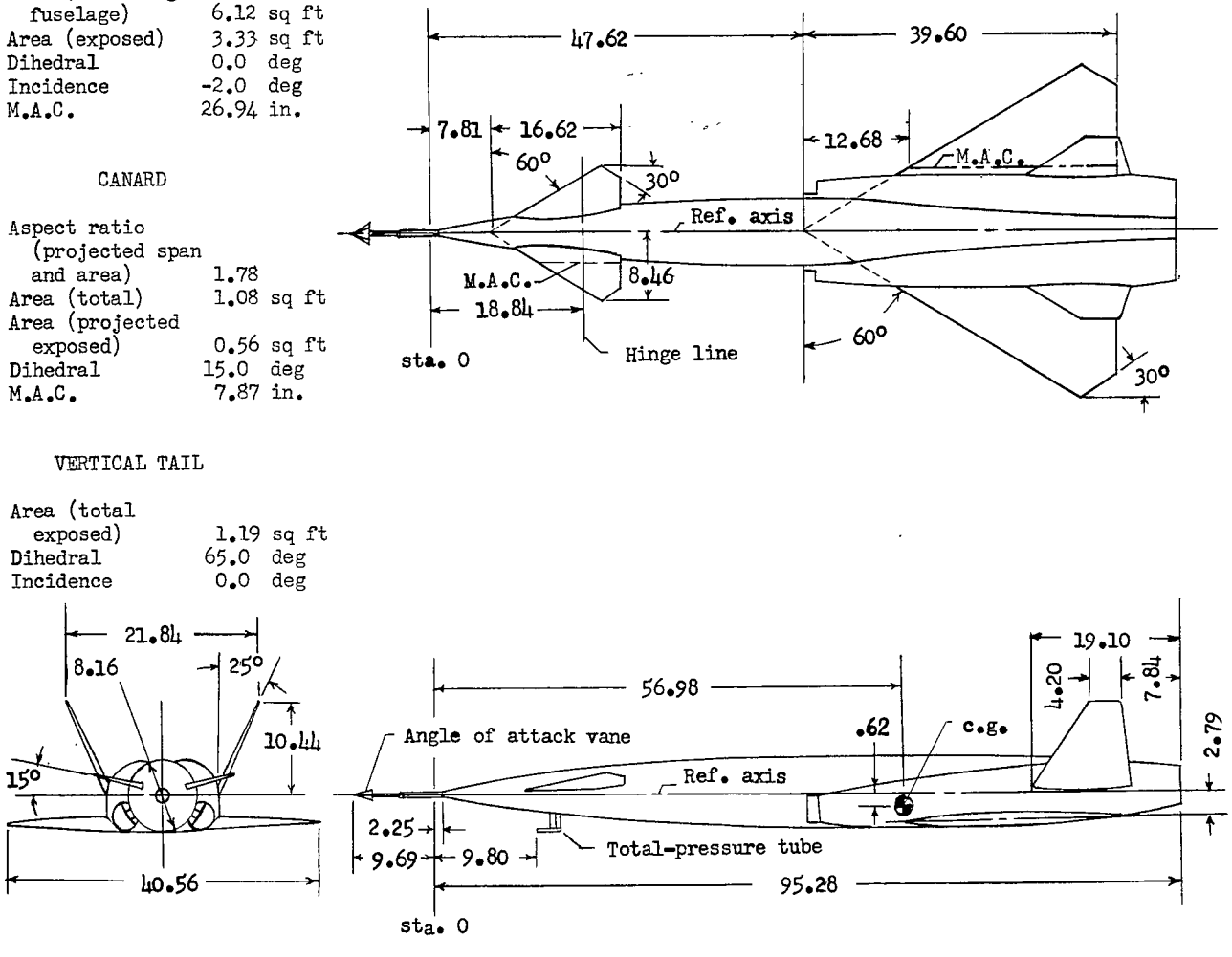

Figure 1.- General arrangement of the model. All dimensions in inches.

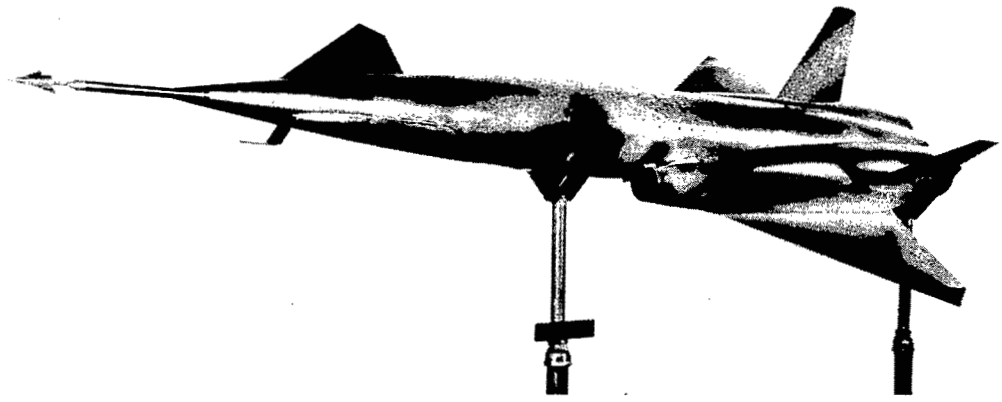

L-75488.1

(a) Three-quarter front view.

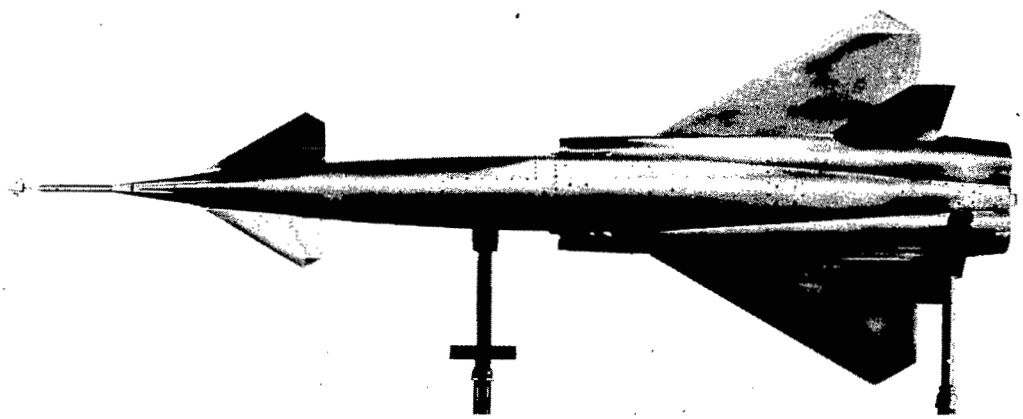

L-77598.1

(b) Top view.

Figure 2.- Photographs of model.

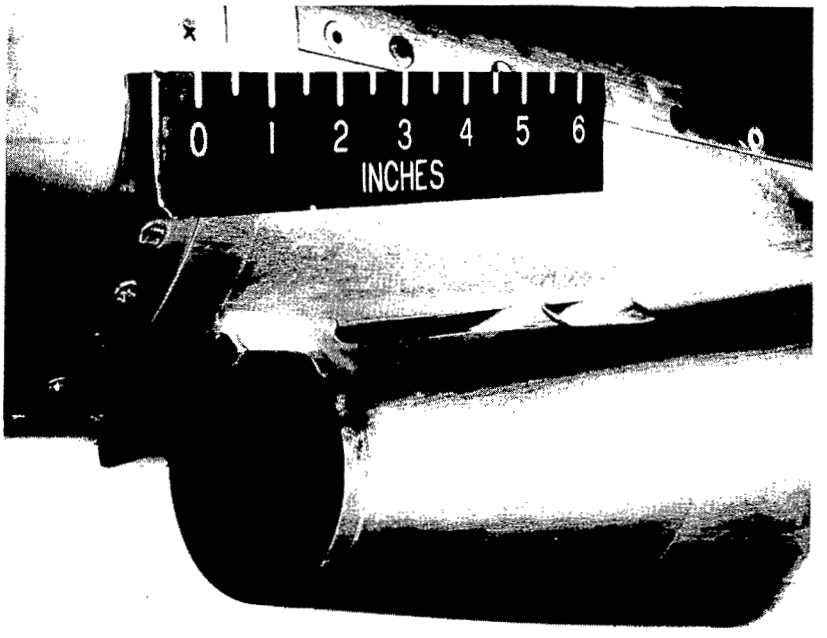

L-75491

(a) Three-quarter front view.

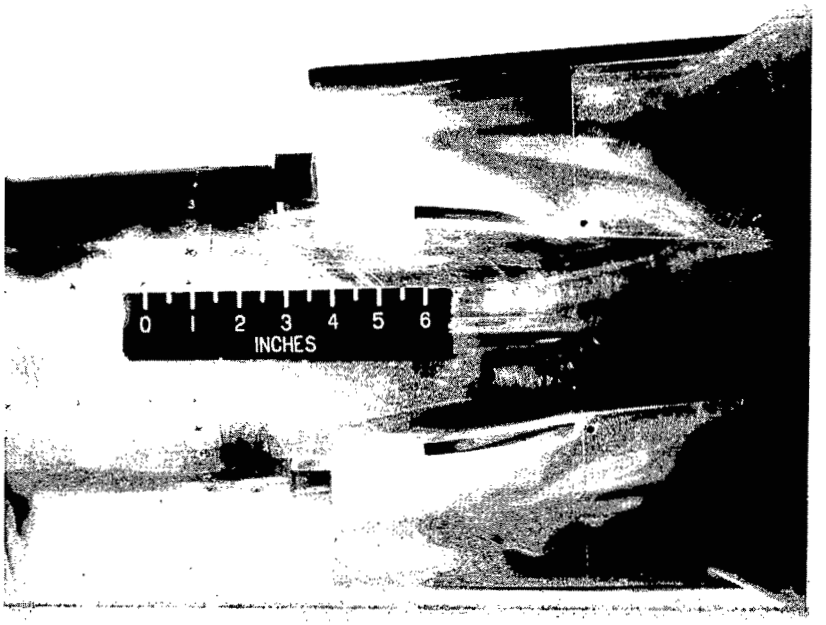

L-75492

(b) Bottom View.

Figure 3.- Inlet and boundary-layer bleed details.

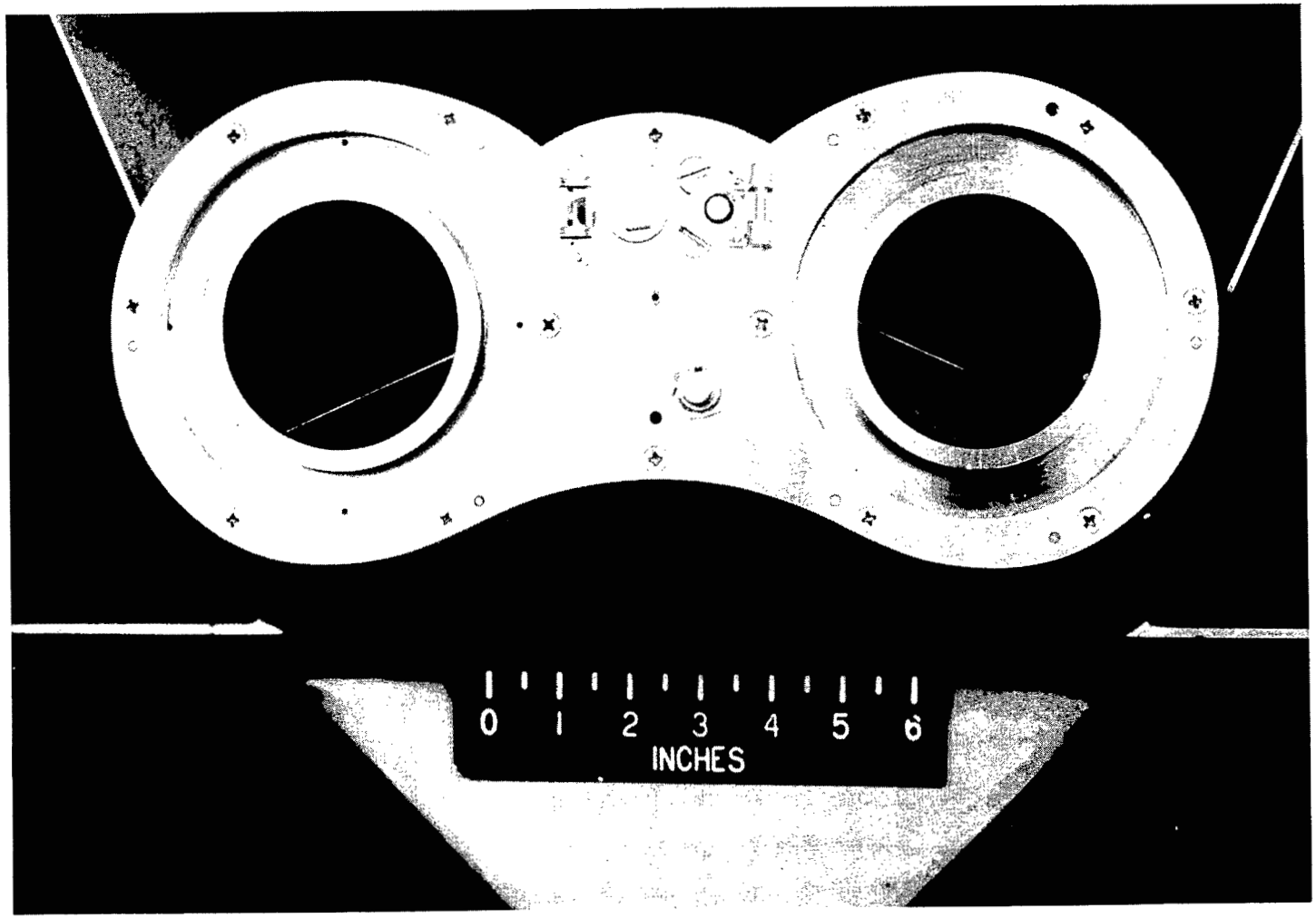

L-75493

Figure 4.- Duct exit and base details.

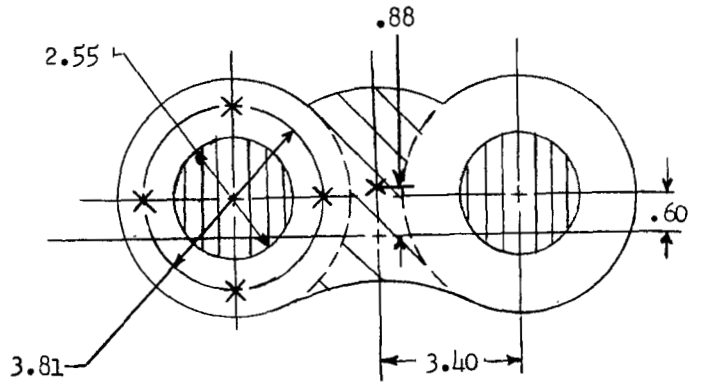

Assumed area of influence of base pressures measured by manifolded orifices, 29.056 sq in.

Assumed area of influence of base pressures measured by center orifice, 8.770 sq in.

Jet exit area, 10.214 sq in.

× Location of pressure orifices

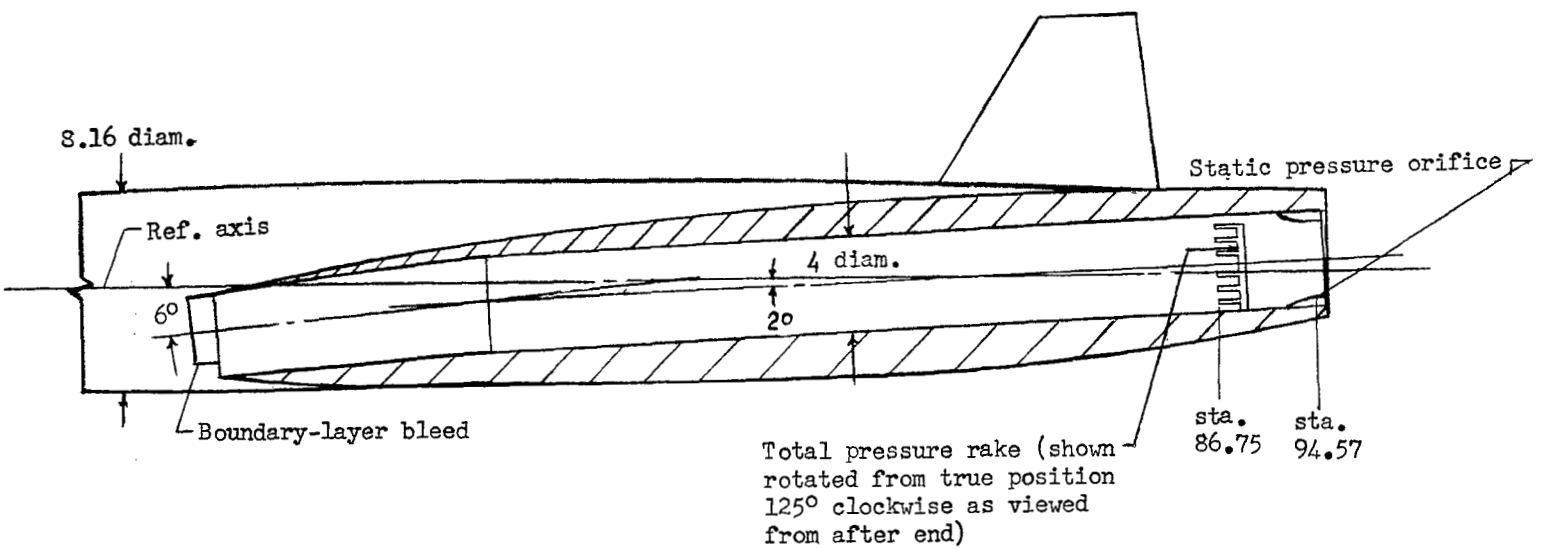

Figure 5.- Duct and base details. All dimensions in inches.

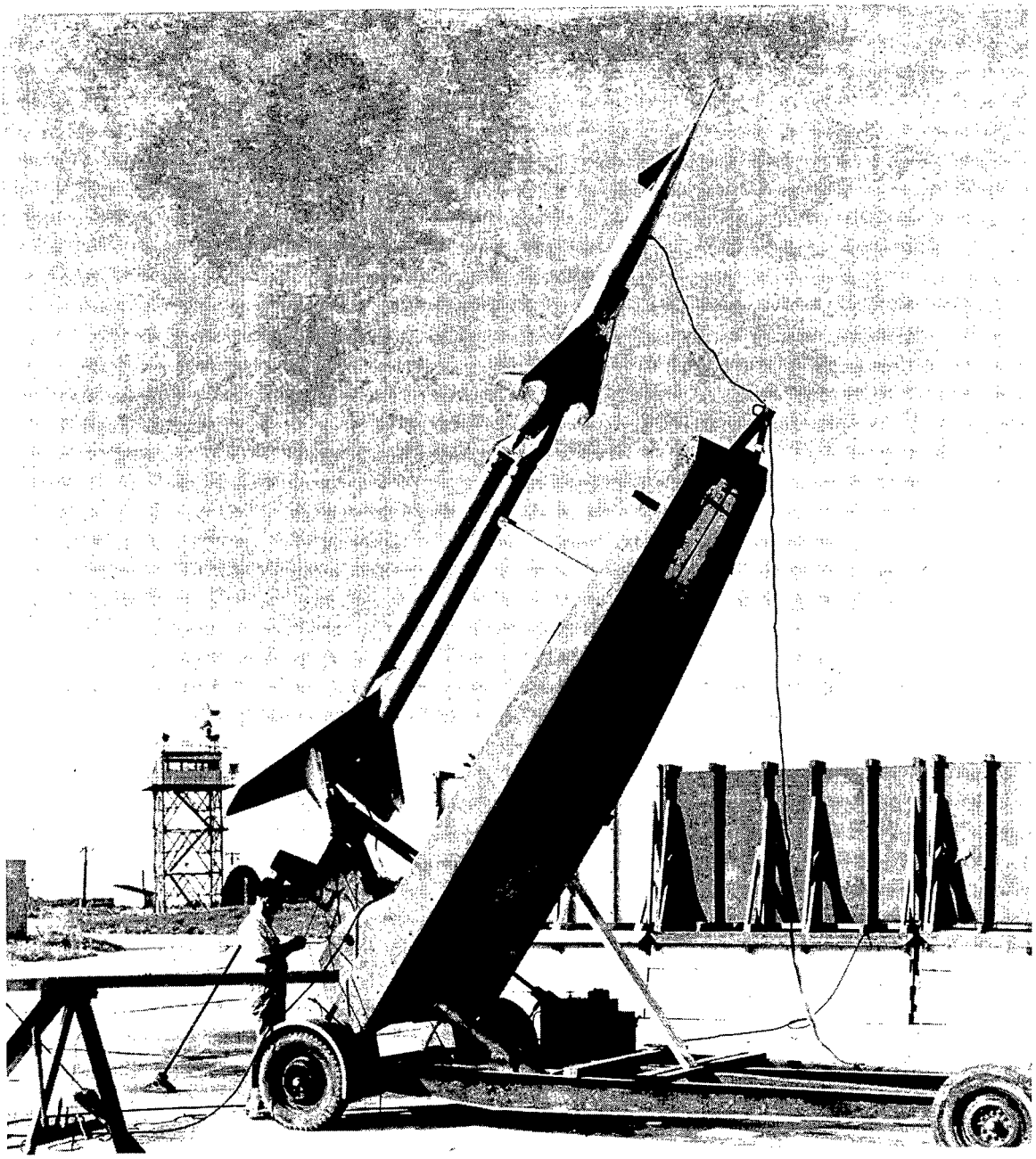

L-75612

Figure 6.- Model-booster combination on launcher.

[redacted]

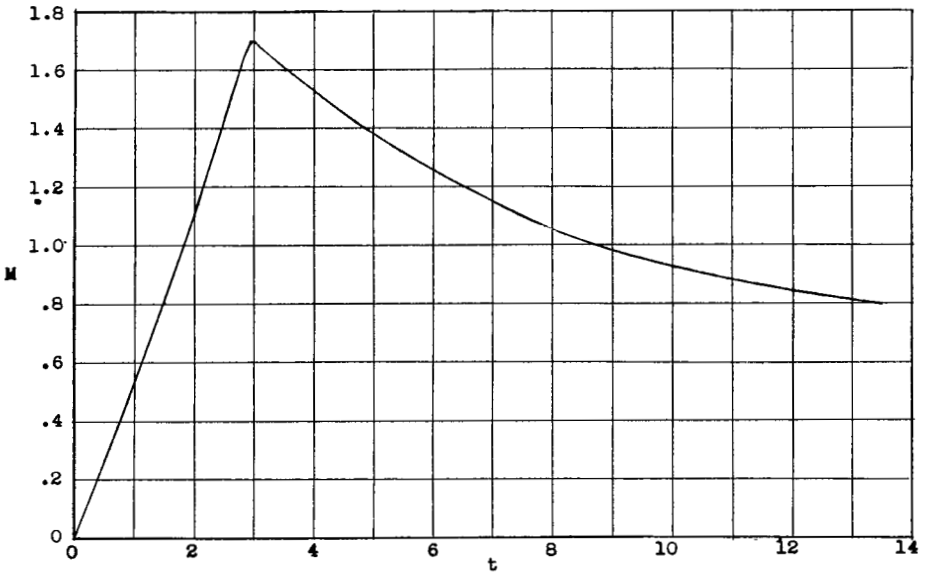

(a) Variation of Mach number with time.

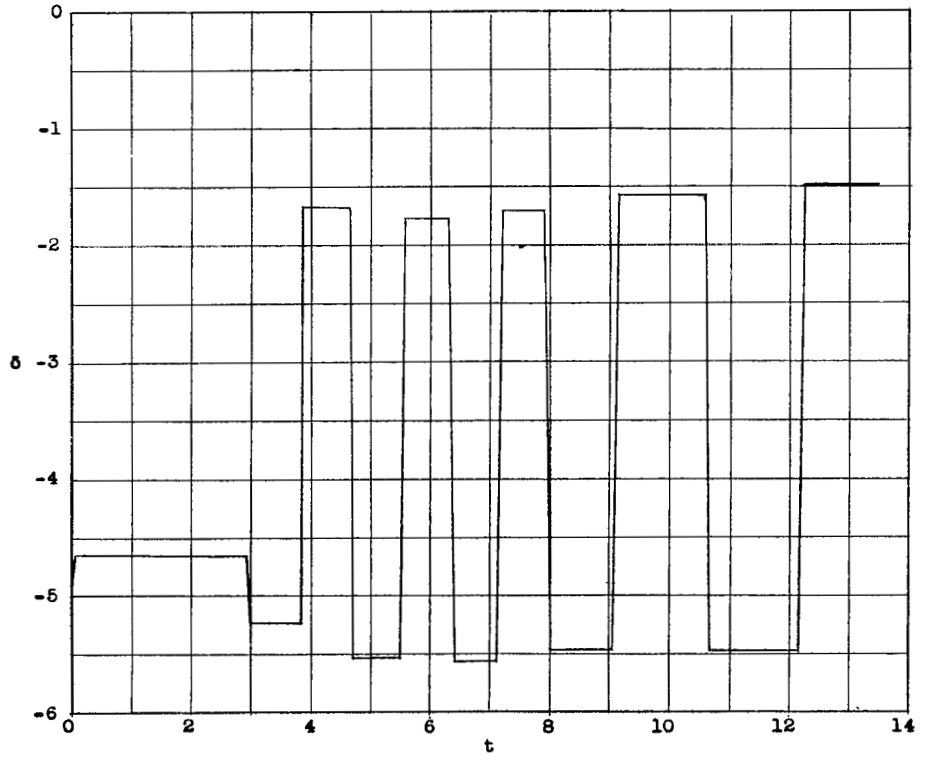

(b) Variation of canard position with time.

Figure 7.- Variation of Mach number and canard deflection with time.

[redacted]

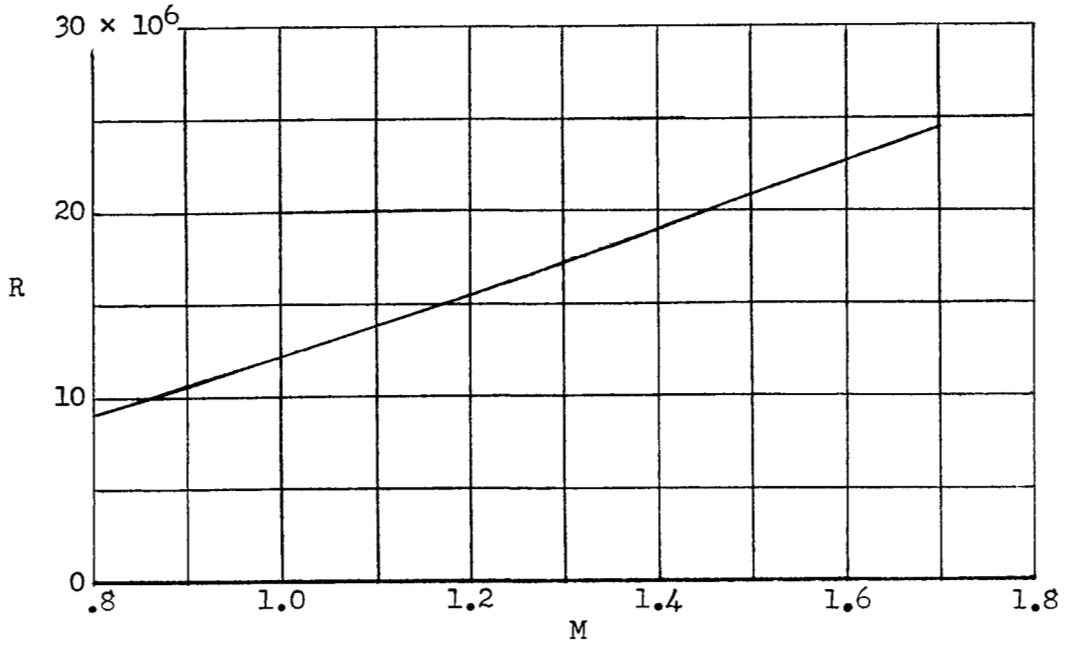

Figure 8.- Variation of test Reynolds number, based on wing mean aerodynamic chord, with Mach number.

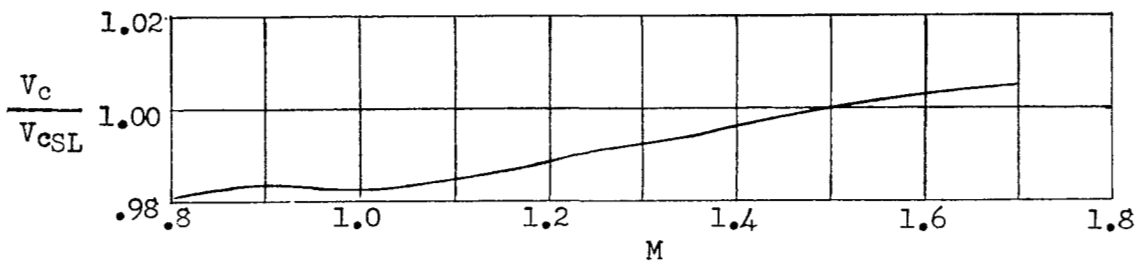

(a) Acoustic-velocity ratio.

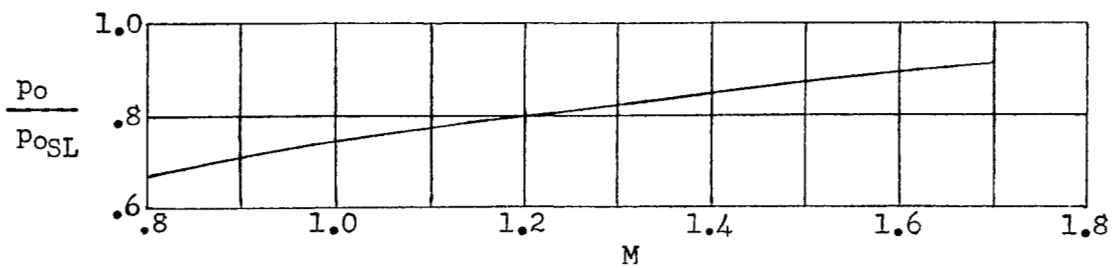

(b) Static-pressure ratio.

Figure 9.- Atmospheric data.

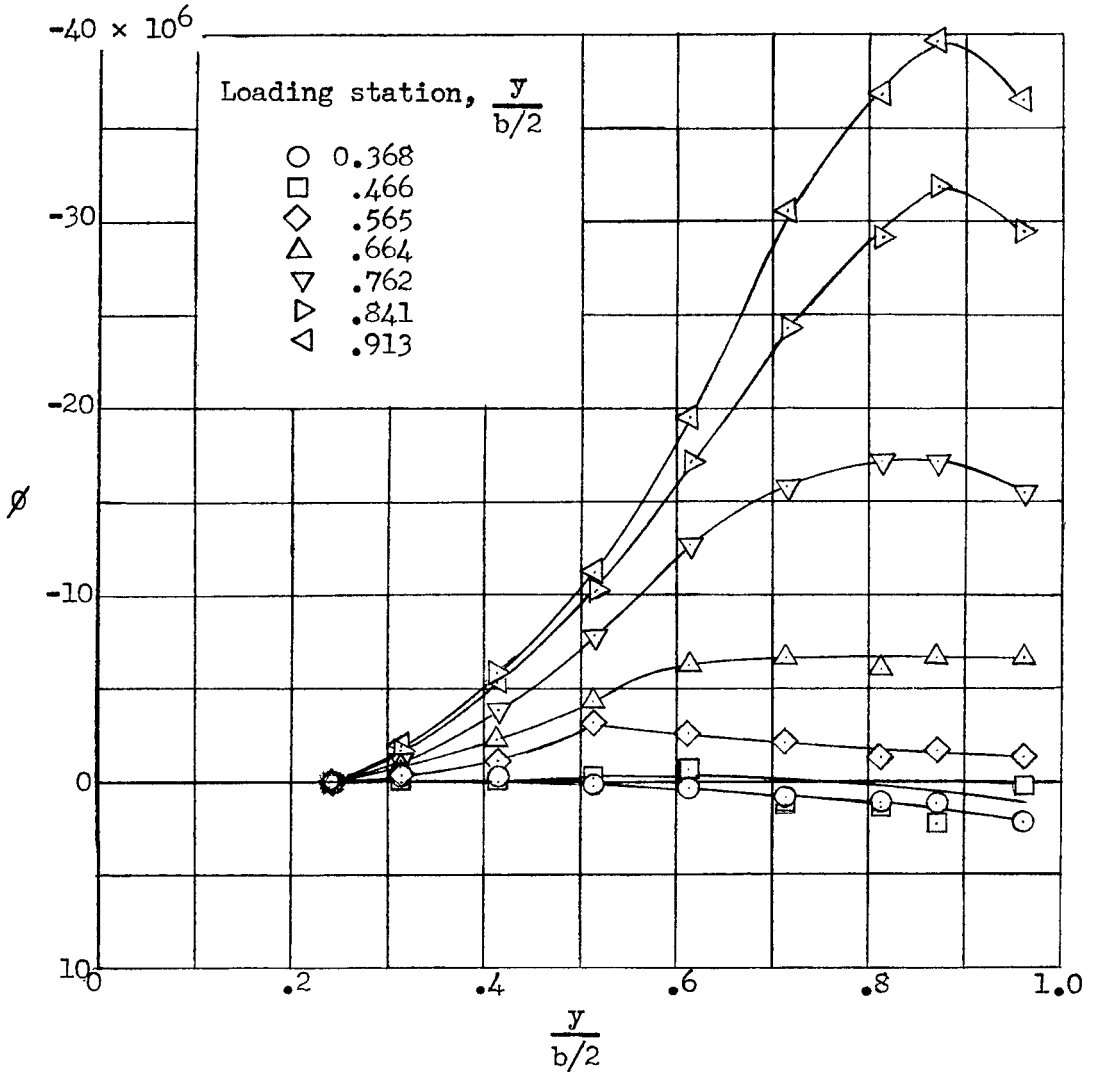

Figure 10.- Twist in the free-stream direction per unit load applied at various stations along the span of the wing on the 50-percent chord line.

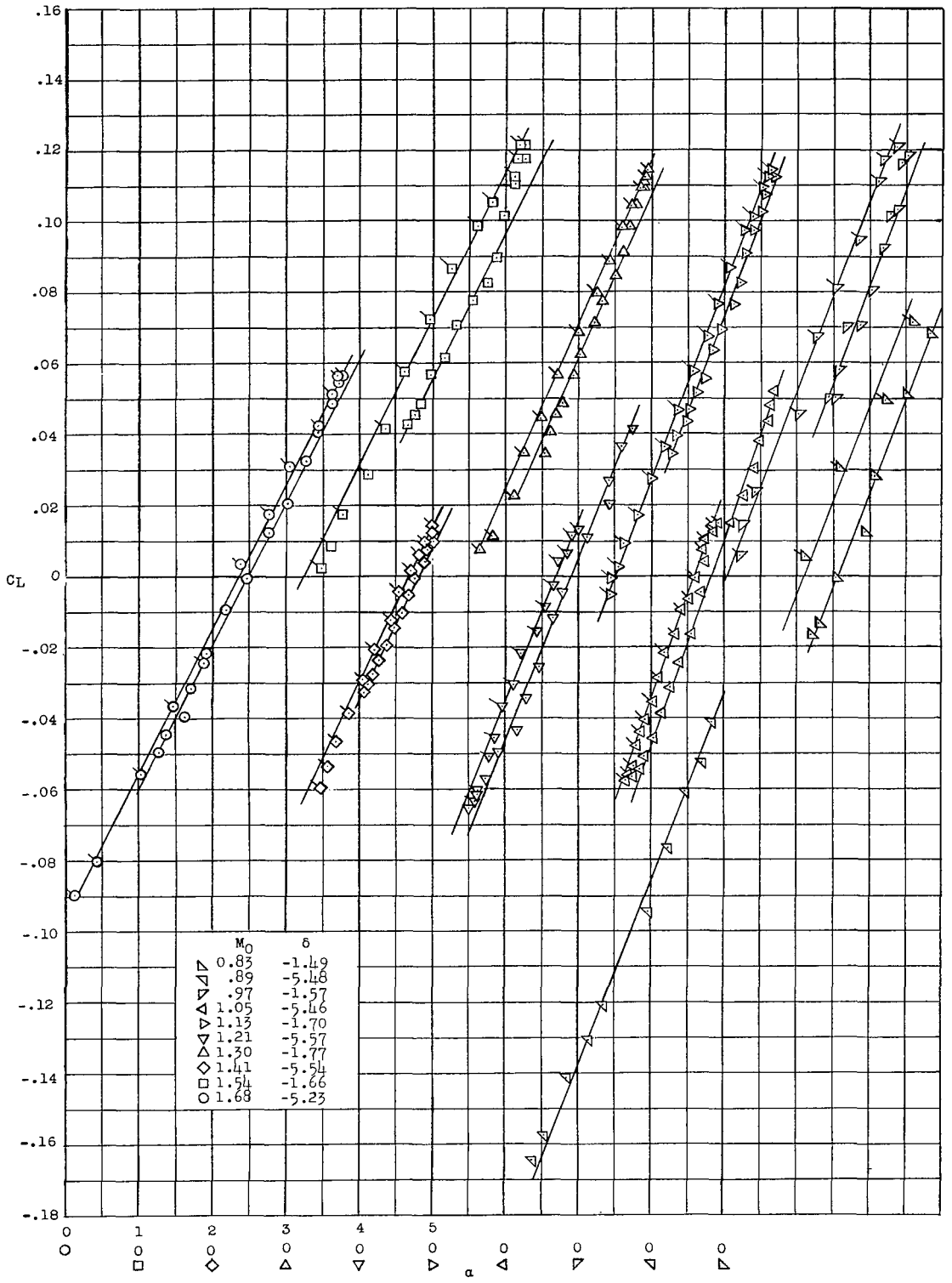

Figure 11.- Variation of lift coefficient with angle of attack. Flagged symbols denote positive values of $d\alpha/dt$.

[redacted]

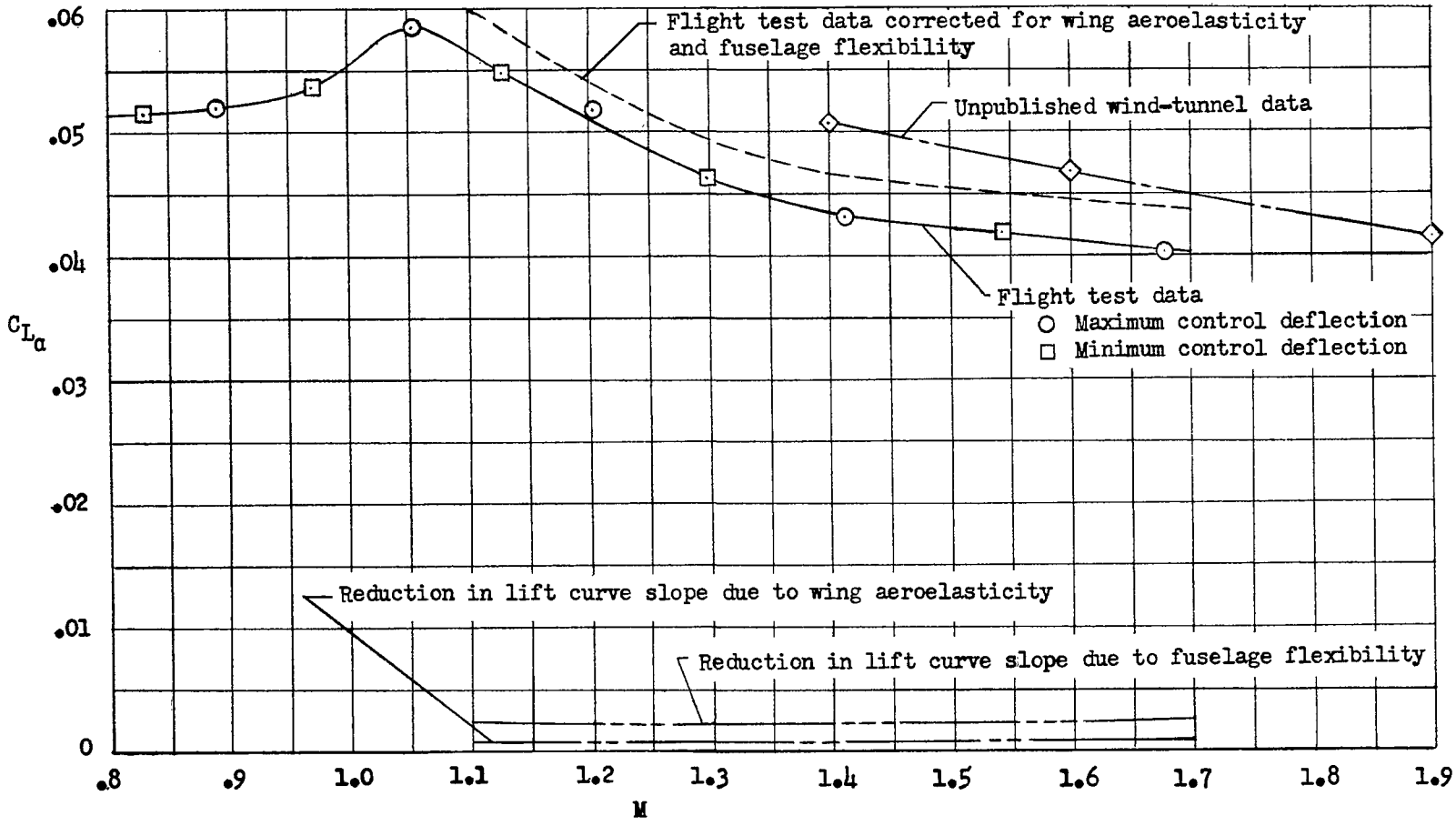

Figure 12.- Lift-curve slope.

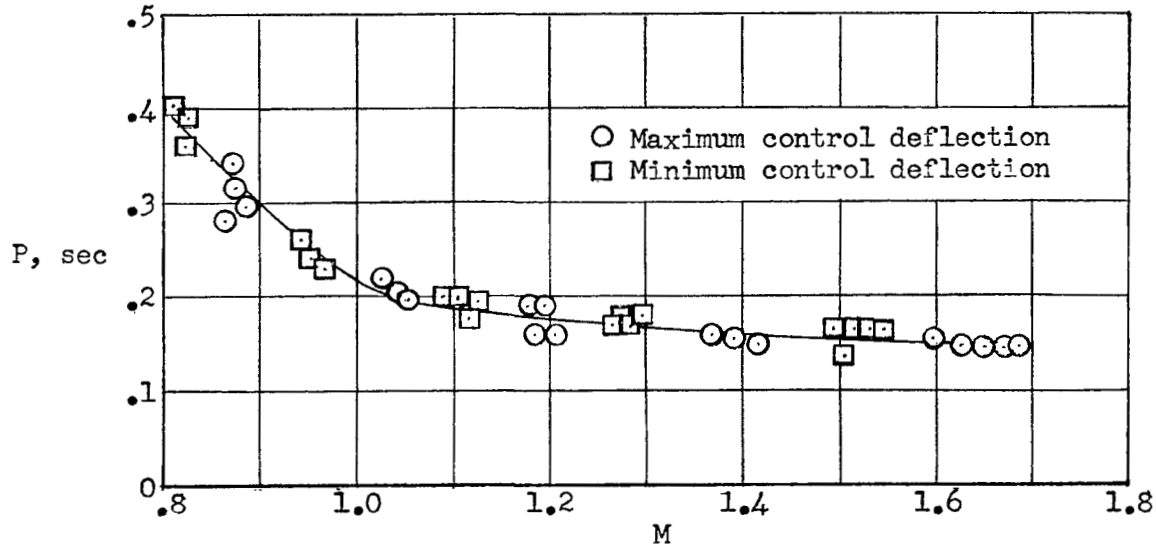

Figure 13.- Period of pitching oscillations.

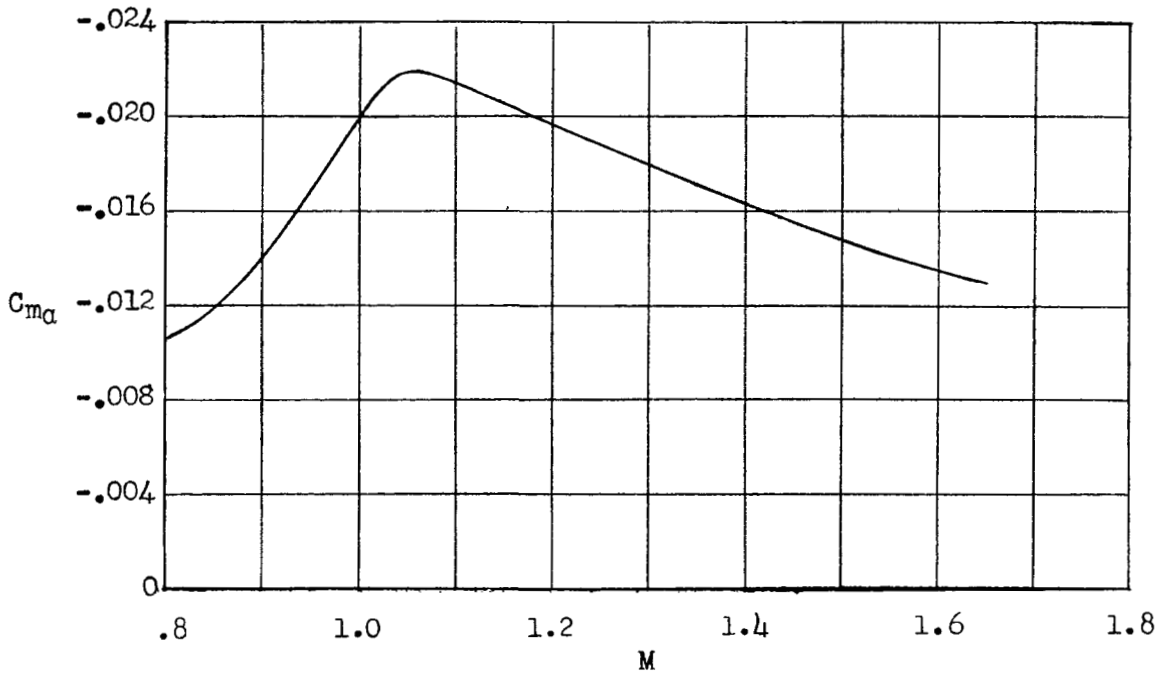

Figure 14.- Static longitudinal-stability parameter C_{m_α}.

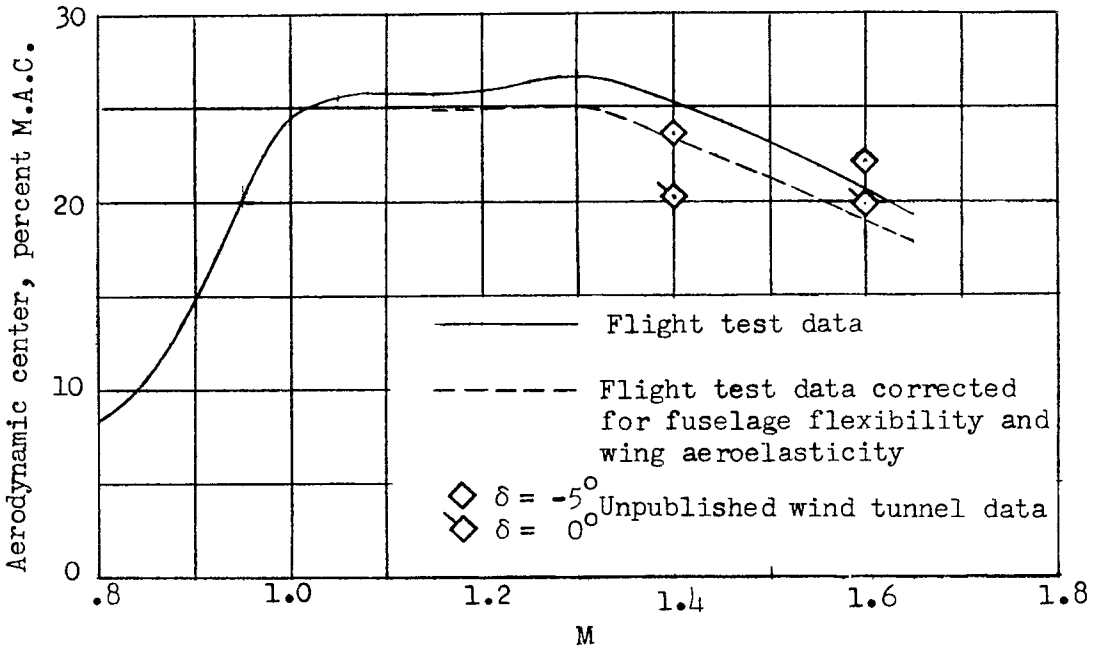

Figure 15.- Aerodynamic-center position.

[redacted]

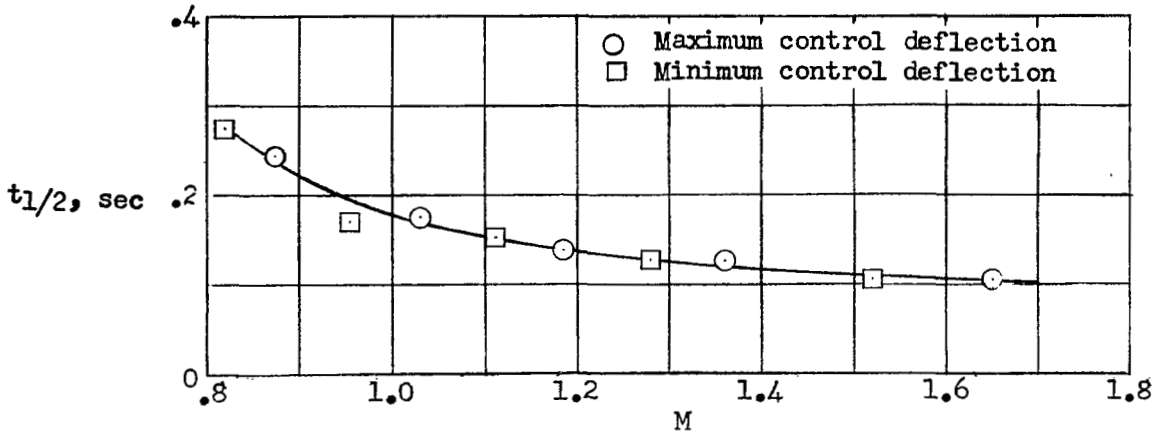

Figure 16.- Time to damp to one-half amplitude.

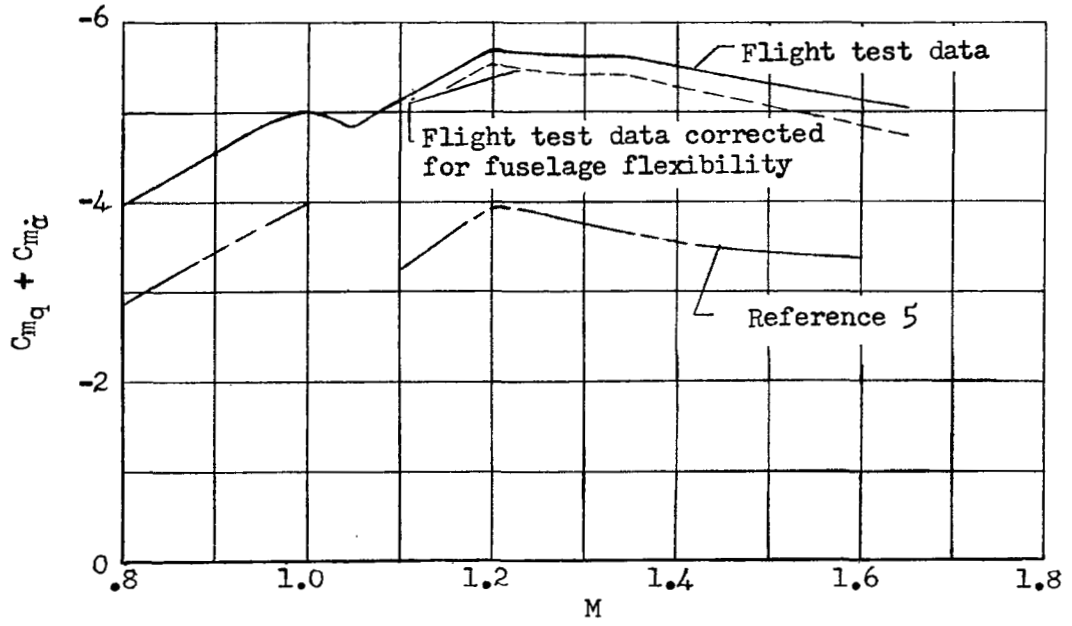

Figure 17.- Variation of damping-in-pitch derivative $C_{m_q} + C_{m_{\dot{\alpha}}}$ with Mach number.

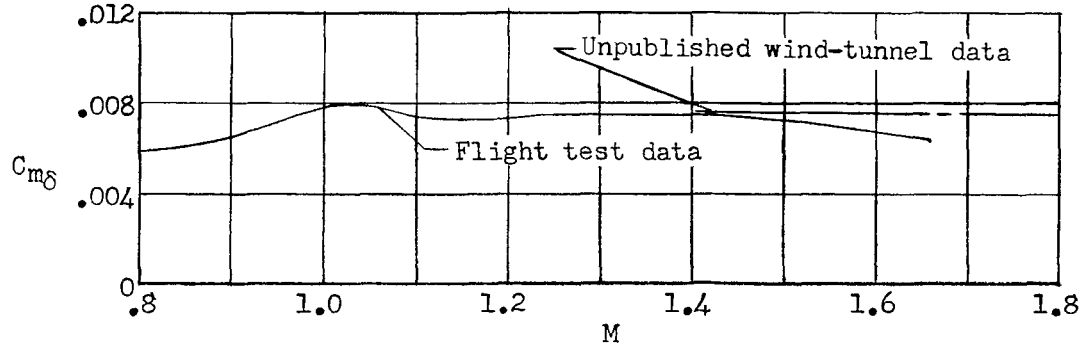

Figure 18.- Effectiveness of canard in producing model pitching moment.

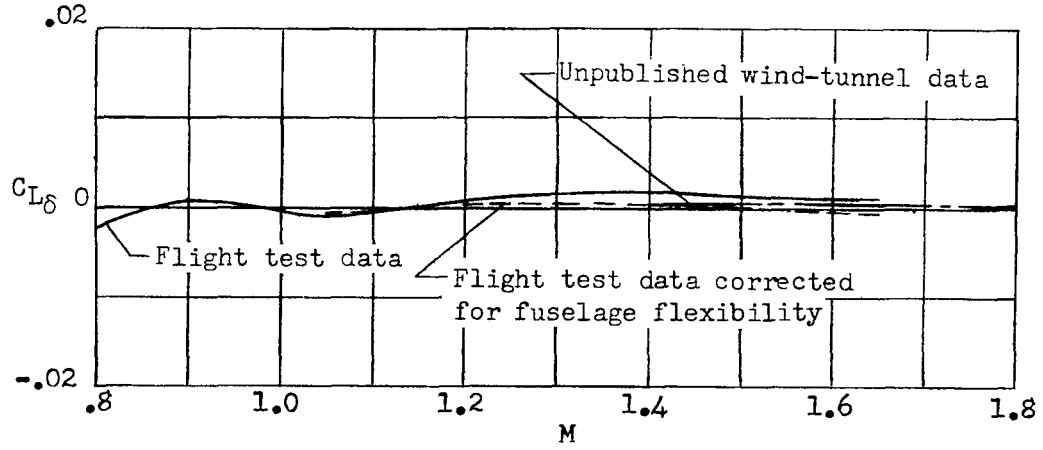

Figure 19.- Effectiveness of canard in producing model lift.

[redacted]

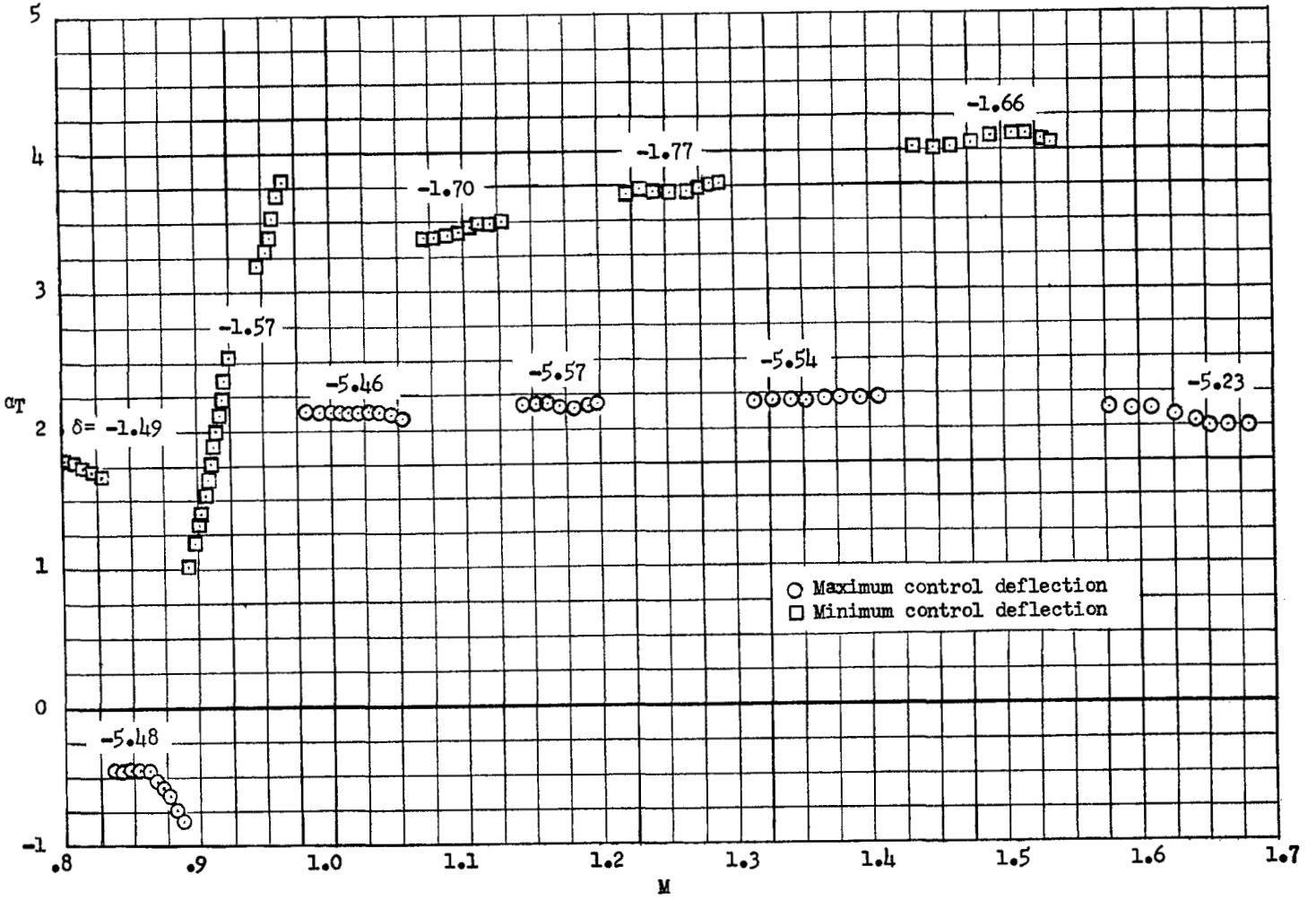

(a) Angle of attack.

Figure 20.- Trim data for varying control position.

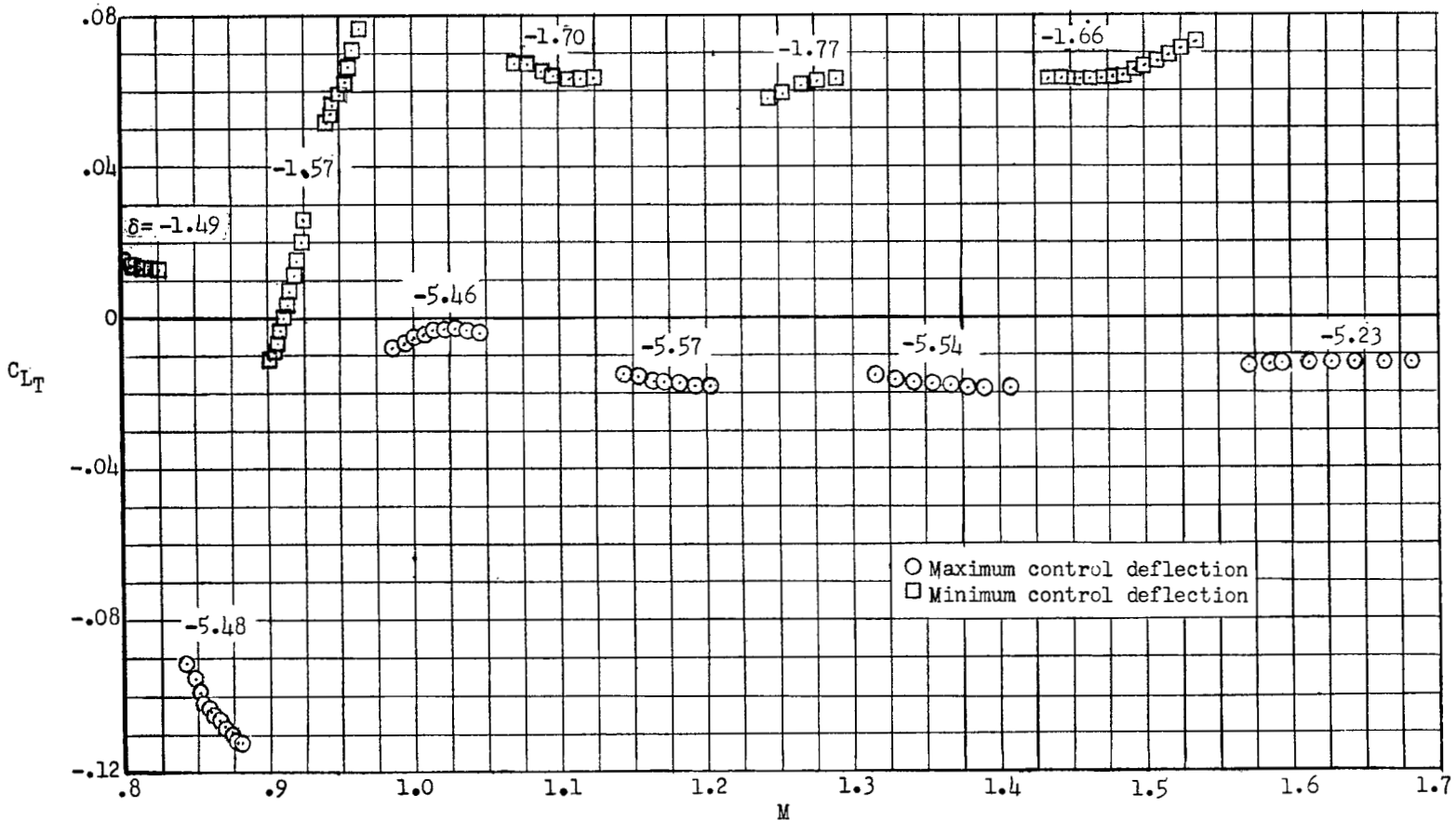

(b) Lift coefficient.

Figure 20.- Concluded.

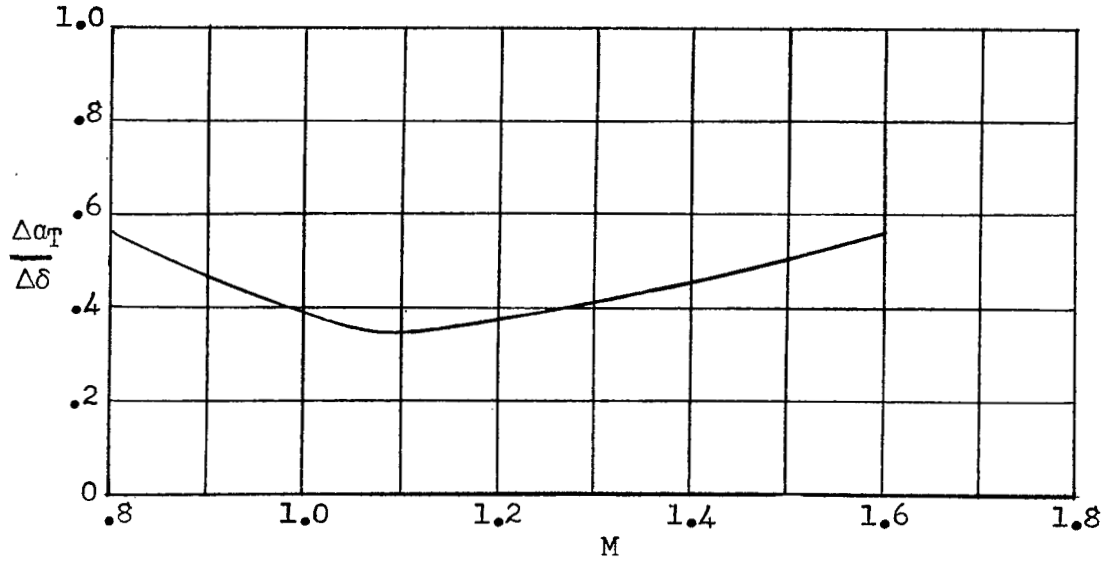

(a) Angle of attack.

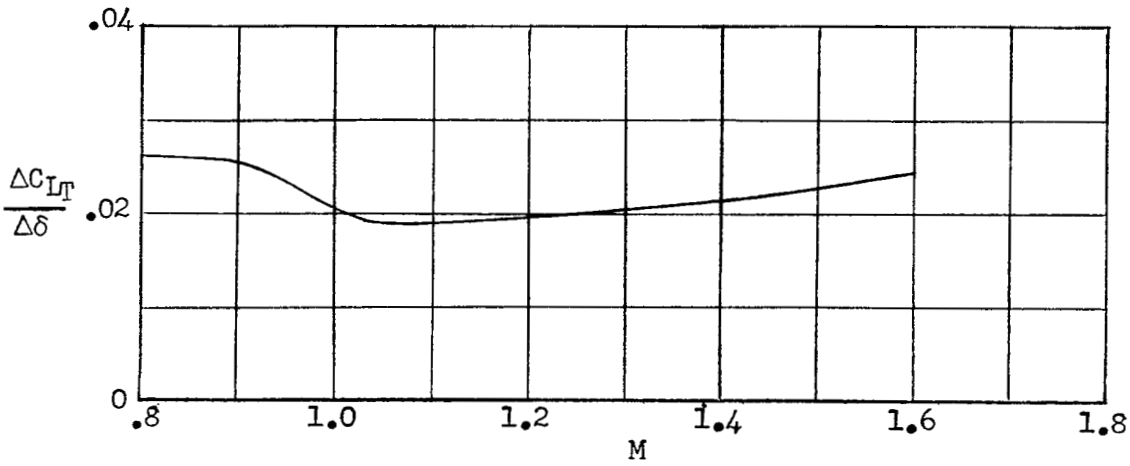

(b) Lift coefficient.

Figure 21.- Change in trim parameters per unit control deflection.

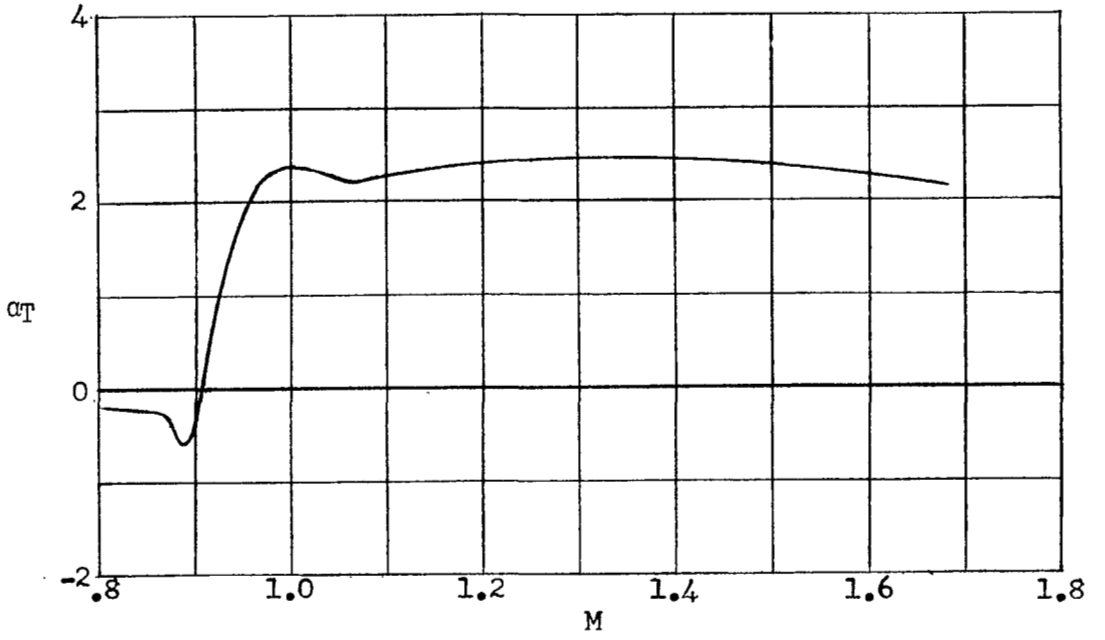

(a) Angle of attack.

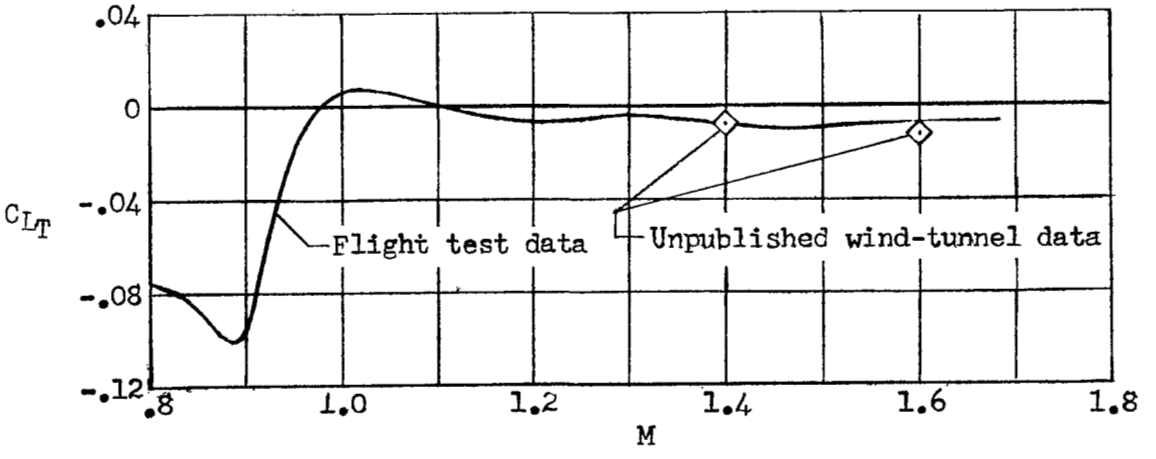

(b) Lift coefficient.

Figure 22.- Trim data for constant control position. $\delta = -5^\circ$.

[redacted]

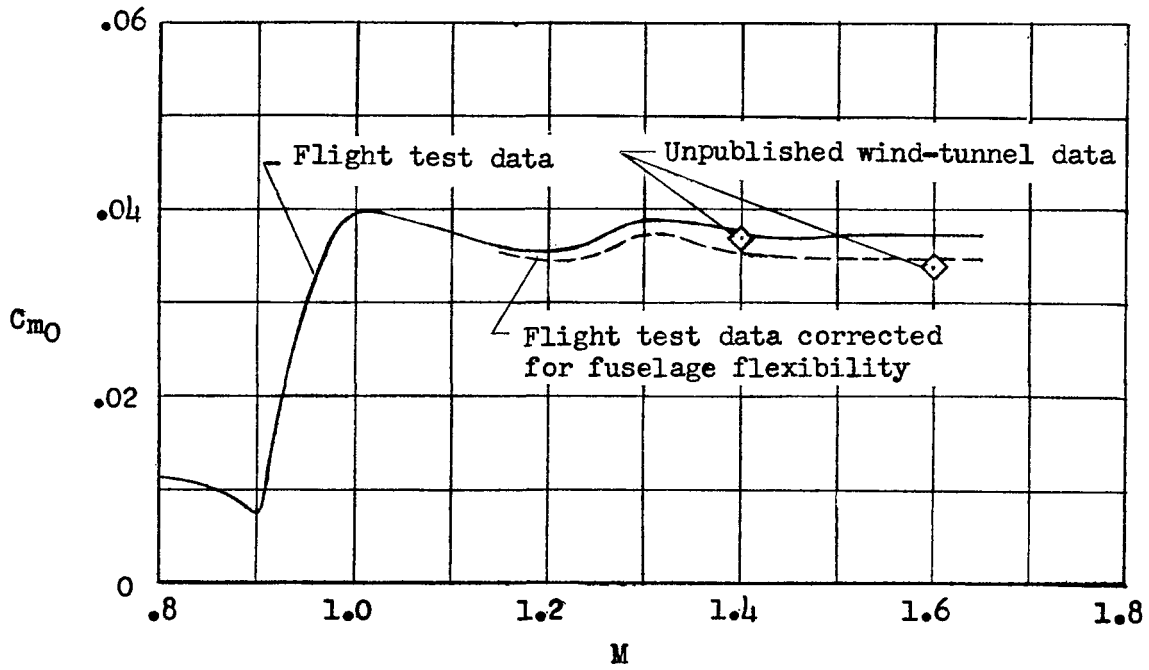

Figure 23.- Variation of pitching-moment coefficient at zero lift and zero control deflection with Mach number.

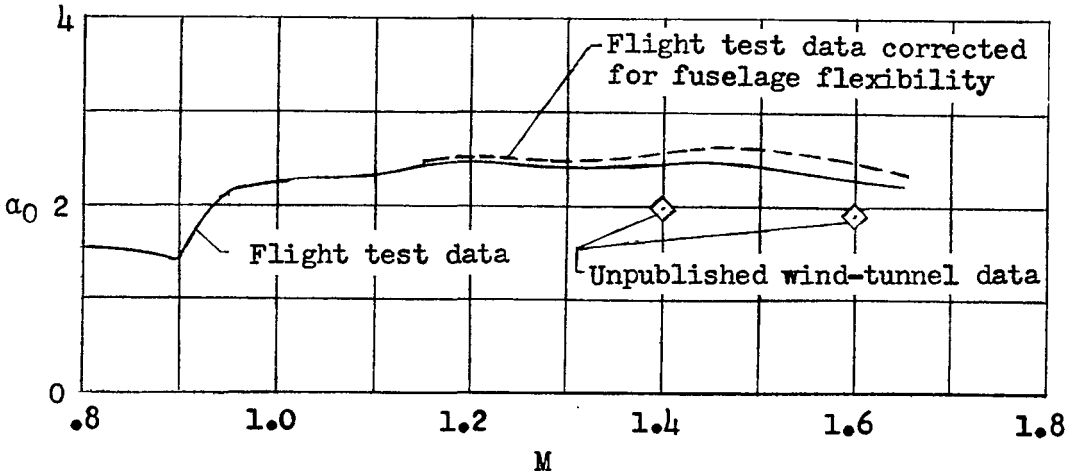

Figure 24.- Variation of angle of attack at zero lift and zero control deflection with Mach number.

[redacted]

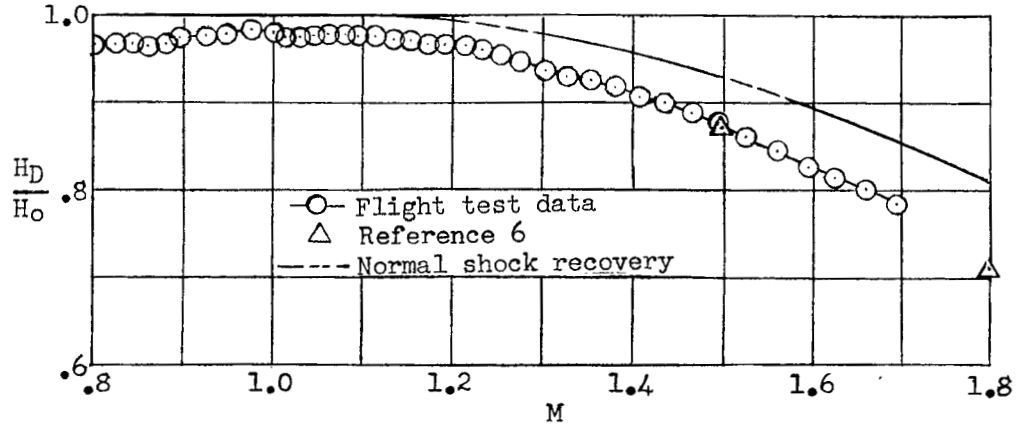

(a) Total-pressure recovery.

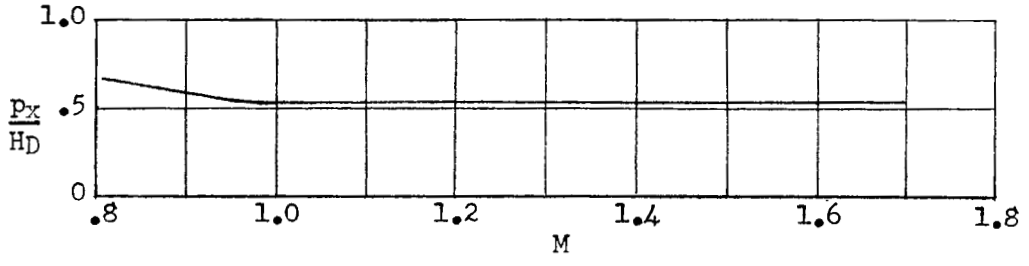

(b) Jet-exit pressure ratio.

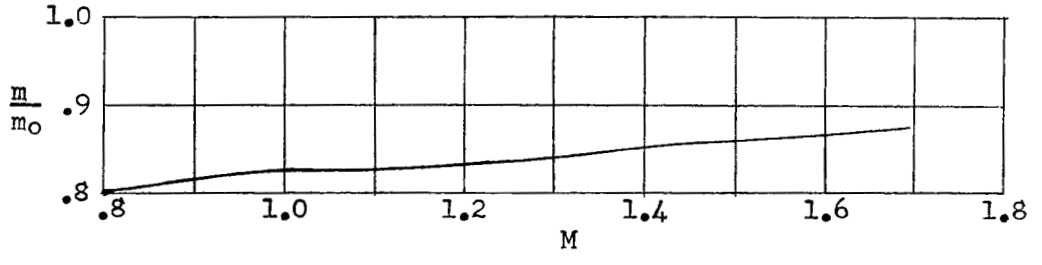

(c) Mass-flow ratio.

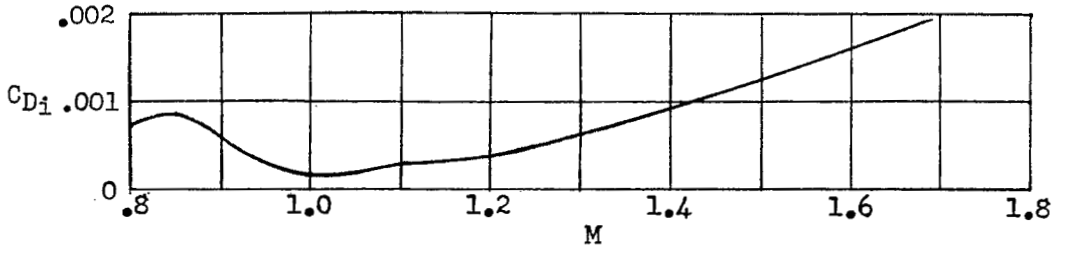

(d) Total internal-drag coefficient.

Figure 25.- Duct-performance data.

[redacted]

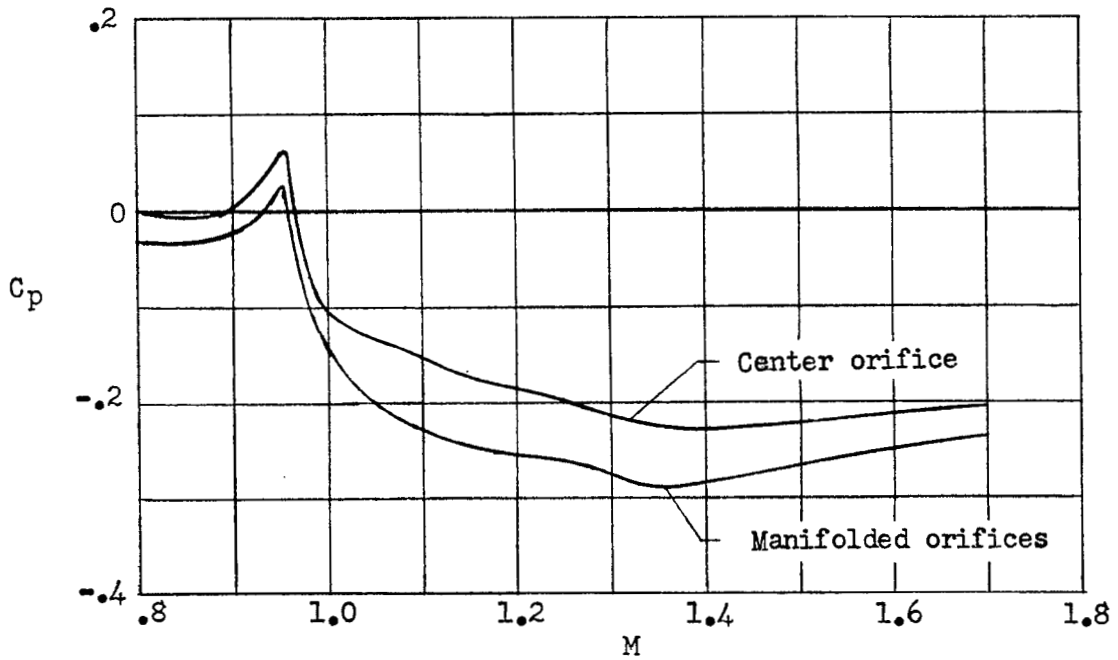

Figure 26.- Variation of base pressure coefficient with Mach number.

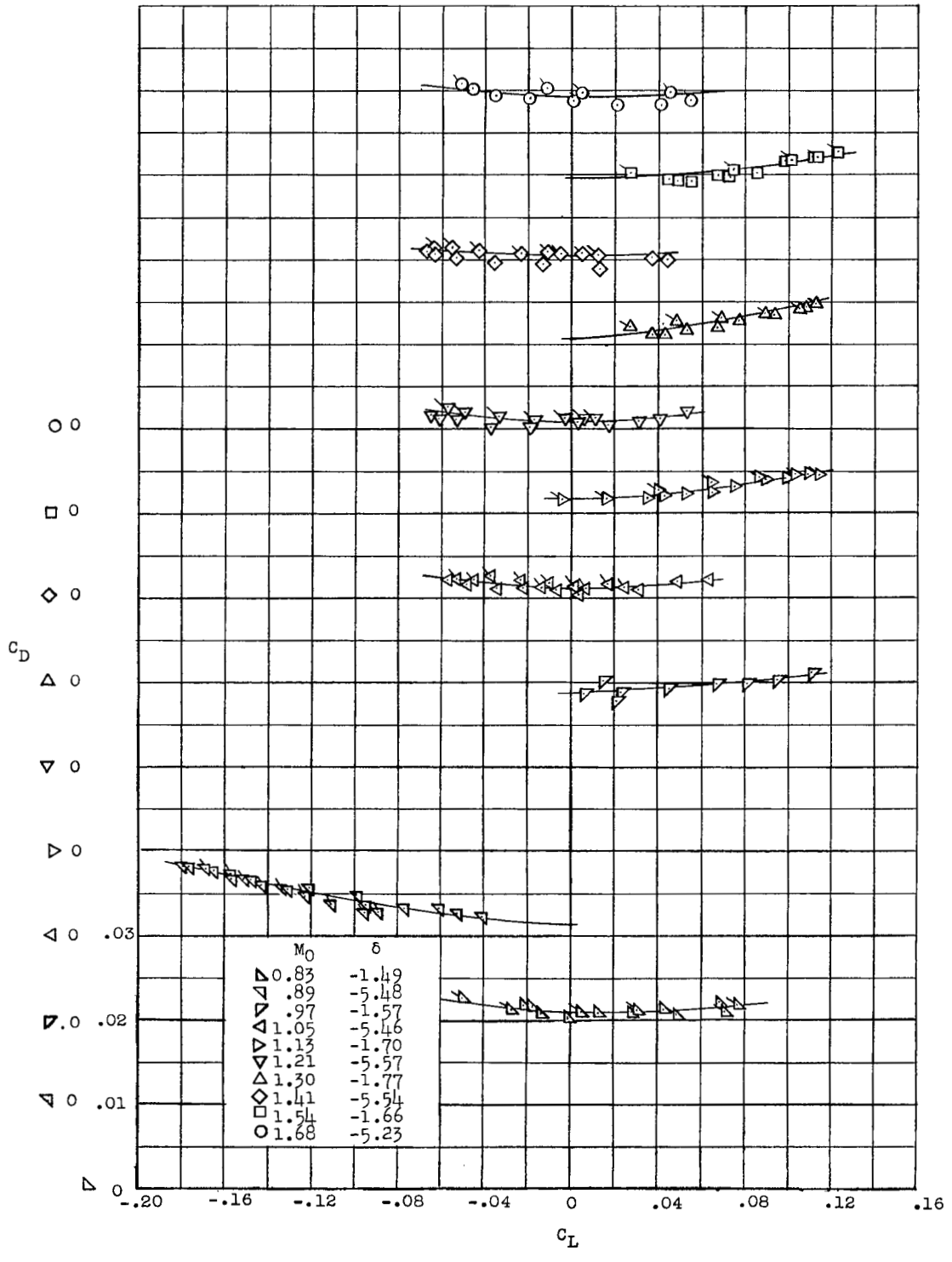

Figure 27.- Variation of total drag coefficient with lift coefficient. (Flagged symbols denote positive values of $d\alpha/dt$.)

[redacted]

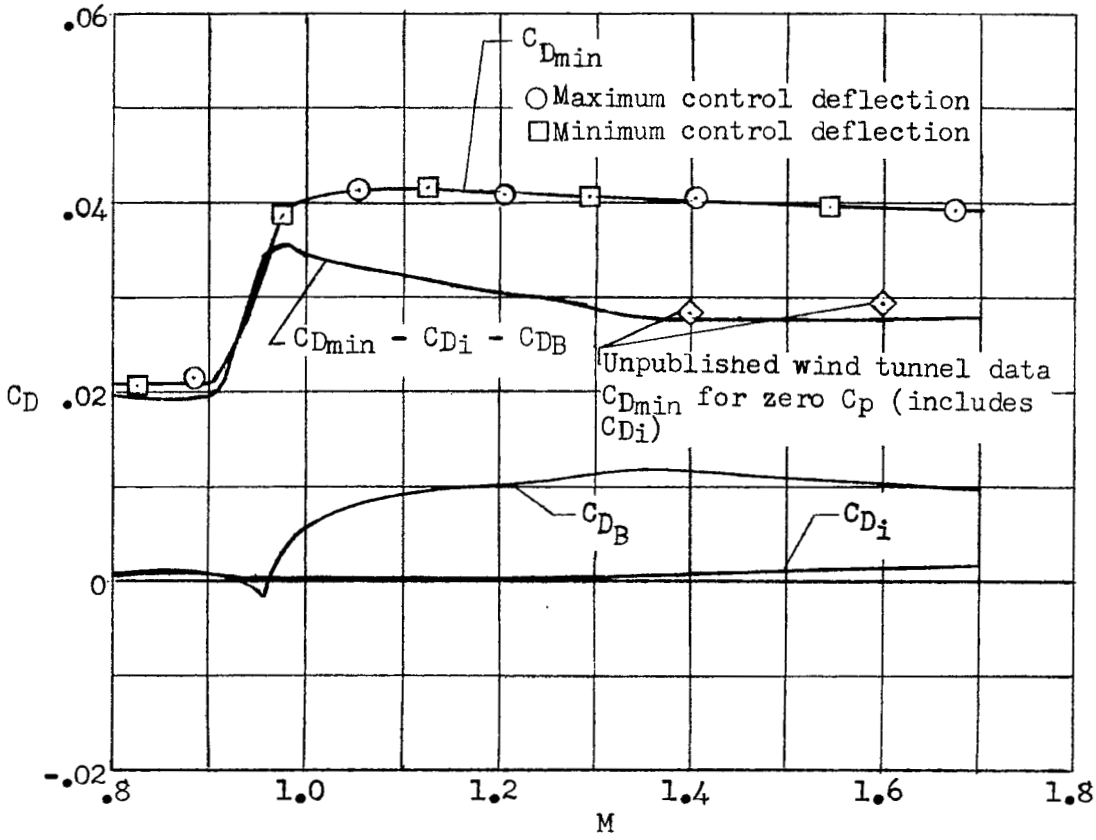

Figure 28.- Variation of drag coefficients with Mach number.

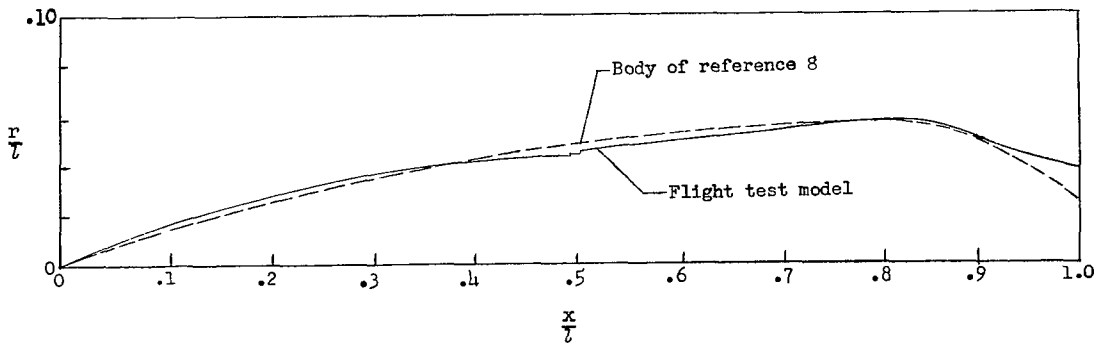

(a) Equivalent body of revolution.

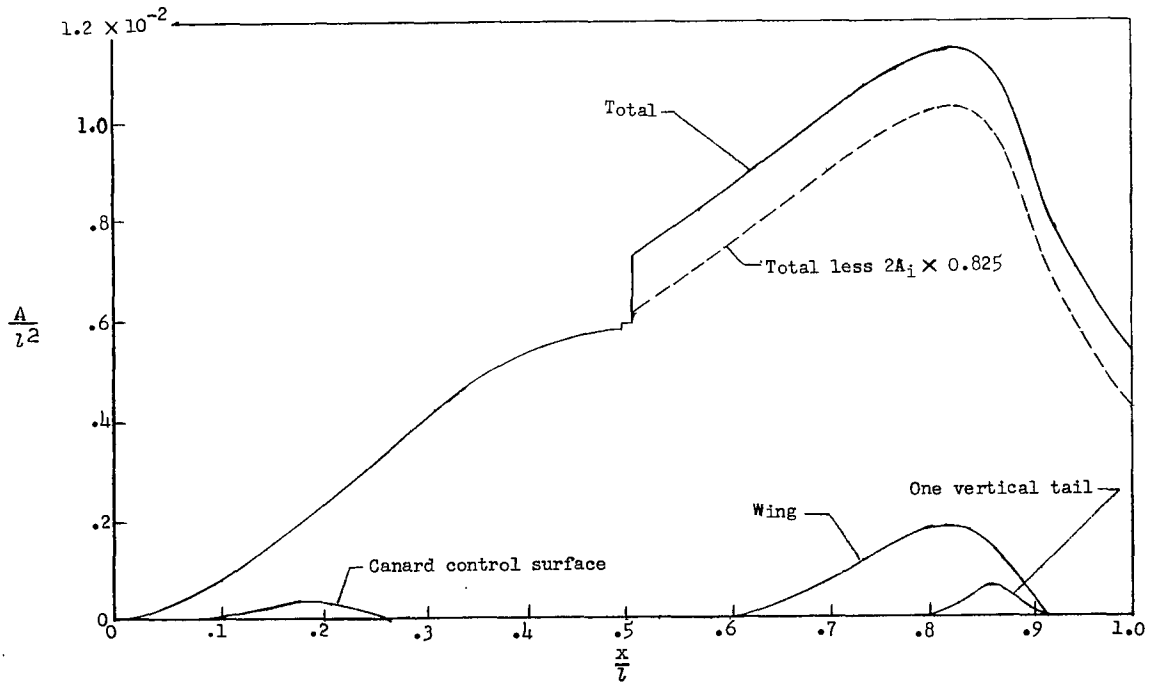

(b) Longitudinal cross-sectional area distribution.

Figure 29.- Cross-sectional area distribution.